Development of a cryogenic index of refraction measuring device

T.P.R. van der Laan, BSc.

Supervisors:
Dr. L Venema
Prof. dr. R.F. Peletier

January 23, 2009

Table of contents

Motivation

In optics, the index of refraction (IoR) of transmissive elements is used to obtain the desired optical behaviour in systems. Two effects are observable when light encounters a transparent medium. Light hitting the medium will be partly reflected at the boundary and the direction of the light beam propagating through the medium will shift (dispersion). Dispersion is used in spectral instrumentation and reflection in imaging systems.

A lot of effort is put forth by industry into determining the IoR to great accuracy. These efforts are however concentrated around room temperatures (293K – 350K).

A black body at 293K (average earth temperature) emits most of its thermal energy at infra-red and sub-millimetre wavelengths. That is why sensitive optical instruments in the infra-red and sub-millimetre wavelength range have to be cooled to cryogenic temperatures; to reduce the background radiation. However, at these temperatures the IoR of almost no material is well known. Yet it is paramount for instrument designers to have access to knowledge of the IoR at cryogenic temperatures.

Other effects hamper the determination of the IoR in the cryogenic temperature range. Most important of these is the coefficient of thermal expansion (CTE). It is equally unknown at these temperatures for most materials, but must be taken into account in any IoR measurement design. New stratagems have to be developed to deal with this problem.

At this time there is one operational test facility for the determination of the IoR at cryogenic temperatures in the world, CHARMS. This instrument has been build by NASA to test the optical materials for the James Webb Space Telescope. Further there are several other groups in earlier stages of development.

Given the current projects and ambitions expressed by the astronomical community, swift and accurate determination of the IoR at cryogenic temperatures is a must. The simultaneous development of several test facilities will, when more are operational, ensure accurate and available IoRs for many materials. ASTRON has decided to join in this effort.

Chapter 2: Index of Refraction theory

The dependence of the IoR on wavelength, at a given temperature, is generally parameterized by the Sellmeier relation. As can been seen from Equation 2.1 this function has asymptotes. The location of the vertical asymptotes are determined by the wavelengths λ_k. These wavelengths correspond to the wavelengths at which photon absorption by the material occur. The accompanying constants B_k give the strength of this absorption.

$$n^2(\lambda) - 1 = \sum_k \frac{B_k \lambda^2}{\lambda^2 - \lambda_k^2} \cong \frac{B_1 \lambda^2}{\lambda^2 - \lambda_1^2} + \frac{B_2 \lambda^2}{\lambda^2 - \lambda_2^2} + \frac{B_3 \lambda^2}{\lambda^2 - \lambda_3^2}$$

Equation 2.1 Sellmeier dispersion relation

The summation in the Sellmeier relation is by necessity truncated after a few terms. Usually this is after the first three terms, which is generally thought to be enough to accurately approximate the IoR over a specific wavelength range of interest. The λ_k's then no longer correspond to the wavelengths of photon absorption, but can be chosen to best fit the data.

At infra-red and longer wavelengths the IoR behaves very smoothly. The terms in the Sellmeier relation corresponding to the λ_k's at much shorter wavelengths, such as ultraviolet, reach their horizontal asymptotes. Their contribution to the IoR in the infra-red range can be parameterized by a single free constant, C_1. This relation is given in Equation 2.2 and for many materials their specific values of the five constants can be found in [Gh98] for one or two temperatures.

$$n^2(\lambda) = C_1 + \sum_k \frac{B_k \lambda^2}{\lambda^2 - \lambda_k^2} \cong C_1 + \frac{B_1 \lambda^2}{\lambda^2 - \lambda_1^2} + \frac{B_2 \lambda^2}{\lambda^2 - \lambda_2^2}$$

Equation 2.2 Infra-red truncation of the Sellmeier relation

The relation of the IoR with respect to temperature is not parameterized in a function. In the literature a derivative is often used to indicate a IoRs dependence on temperature. This derivative, called a thermo-optic coefficient (TOC), is specific to a certain temperature or temperature range. The reported temperatures are usually around room temperature. In the case that the TOC is computed over a larger temperature range, it must be regarded as a global value. The TOC, like the IoR, is also dependent on wavelength.

Section 2.1 Goal

Our goal in this study is to develop a method able to measure the IoR of solids within the following framework:

- wavelength range 300nm - 25µm
- temperature range 20K – 300K
- accuracy to at least the 5th decimal place

We wish to fill the parameter space of wavelength and temperature as densely as possible, while maintaining the stated accuracy for every position.

Chapter 3 World wide efforts

An article search on the World Wide Web has identified other research groups making efforts to determine the IoR at cryogenic temperatures. The most noted of these is CHARMS located at NASA. The other groups are in Italy, Cambridge and Japan. A description of the main method described below, the deviation method, will be given in the next chapter.

NASA CHARMS

CHARMS is a working refractometer which operates in the infra-red to ultraviolet wavelength range and down to a temperature of 15K. Most of the equipment has been build into a cryostat vacuum chamber. The set-up has one moving component, a mirror, while the prism remains fixed in place. The prism angle is also measured in-situ as part of the data acquisition procedure. Results have been published for several glasses with accuracies of 10^{-5} or better.

An interesting observation by CHARMS has been the existence of a saturation temperature. Below this temperature, which is material dependent, the IoR will no longer change [Le05]. This temperature can be as high as 65K.

Italy

We have found two groups in Italy.

The first group uses the 'classic' minimum deviation method. Demonstrative measurements have been conducted between temperatures of 105 and 293K and wavelengths from 480 to 894 nm. The measurement uncertainty is 3.10^{-5}. To maintain good thermal uniformity the prism has been sandwiched between two aluminium plates, which are in turn fixed to three thermal contacts. Thermal uniformity is of course an important parameter of all measurement set-ups. This group wishes to convey their extra effort in maintaining it.

Even thought as of yet this approach has a very limited parameter range, the authors stress its simplicity [Va08].

The second group uses the modified minimum deviation method. Here the first prism surface is normal to the light beam. This set-up has the advantage that the prism can be fixed into place. Of the set-up only the fixed prism and a movable retro-reflective mirror are placed inside a cryostat unit. Overall this system will be relatively cheap. The deviation angle corresponds with the mirror rotation angle. It will be capable of measurements between temperatures of 100K to 300K and wavelengths of 0.4 to 1.7 micron. First light was expected for the end of 2008 [Sp08].

Japan

A gonio-type refractometer has been customized especially for these measurements. This refractometer is fitted with a double gear system, which maintains equal incident and exit angles. The set-up works with the minimum deviation principle. Only the prism is placed in a cryostat chamber. This group measures the offset from the IoR at 293K for temperatures down to 80K. The wavelength range reported is 365.0 to 3298 nm. Accuracies of 10^{-4} have been reached [Ya06].

Cambridge

Finally a measurement on Ohara glass S-FTM16 has been found which was conducted on The Cryogenic Refractometer built by J. Palmer and collaborators [Wo80], which is based on the modified minimum deviation method. The temperature range is 77K to 298K and the wavelength range is 0.6 µm to 2.6 µm. No measurements were possible in the discussed set-up for temperatures between 100K and room temperature. No further indication of use of this set-up for other materials was mentioned [Br04].

Table 3.1: Overview of the parameter space covered by the different groups

	Temperature range	Wavelength range	Accuracy (10^{exp})
CHARMS	15-320K	400nm - 5.6 µm	-5 / -6
Italy 1	105-293K	480nm - 894 nm	-5
Italy 2	100-300K	400nm - 1.7 µm	-5
Japan	80-293K	365nm - 3.298 µm	-4
Cambridge	77-298K	600nm - 2.6 µm	-5
ASTRON	**20-300K**	**300nm - 25 µm**	**-5**

Chapter 4: IoR measurement methods, keeping temperature constant

In this chapter we will focus on methods which are capable of measuring the IoR over a specific wavelength range, while keeping the temperature constant. IoR measurements at room temperature follow this approach. Previous work done at ASTRON [Be07] has presented two such methods which are also capable of measuring the IoR at cryogenic temperatures; the minimum deviation refractometry method and a method based on the Fabry-Pérot interferometry principle.

Section 4.1 Minimum deviation refractometry

Any light beam passing through a prism will be refracted twice (Figure 4.1). The resultant deviation angle is dependent on the IoR. There exists a minimum deviation angle for each prism. This angle is dependent on the IoR and apex angle of the prism. Finding the minimum deviation angle and solving for the IoR has two great advantages over finding and solving the system for an arbitrary deviation angle. Working with the minimum deviation angle simplifies the geometry of the system and the dependence on initial incident angle is lost. The tolerance on the remaining apex angle also relaxes.
We will derive the equations which govern the deviation angle and show the minimum deviation equation, Equation 4.1.[He02]

$$n = \frac{\sin((\theta_{Dev,\min} + \theta_{apex})/2)}{\sin(\theta_{apex}/2)}, \quad n \equiv \frac{n_{material}}{n_{ambient}}$$

Equation 4.1 IoR minimum deviation relation

Snell's law states that at each boundary between two media the angle of the light beam in the refractive medium is related to the incident angle, given the IoRs of both media.

$$n_1 \sin(\theta_1) = n_2 \sin(\theta_2)$$

Equation 4.2 Snell's Law

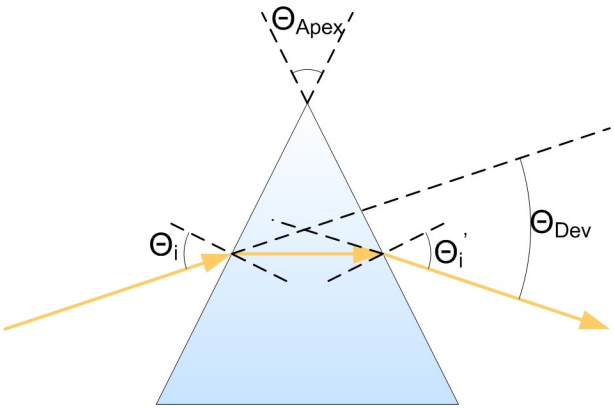

Figure 4.1: schematic overview of the minimum deviation refractometry method

The derivation of Equation 4.1 goes as follows:

$$\theta_{Dev} = (\theta_{i1} - \theta_{t1}) + (\theta_{t2} - \theta_{i2})$$
$$\theta_{apex} = \theta_{t1} + \theta_{i2}$$
$$thus$$
$$\theta_{Dev} = \theta_{i1} + \theta_{t2} - \theta_{apex}$$

Equation 4.3

θ_{i1}, θ_{t1}, θ_{i2} and θ_{t2} are the incoming and exiting angle for the first and second refraction.
Snell's law enables further determination of θ_{t2}, the final angle outside the prism, in terms of θ_{i1} and θ_{apex}.

$$\theta_{t2} = \sin^{-1}(n\sin(\theta_{i2})) = \sin^{-1}(n\sin(\theta_{apex} - \theta_{t1}))$$
$$= \sin^{-1}\left[n\left(\sin(\theta_{apex})\cos(\theta_{t1}) - \cos(\theta_{apex})\sin(\theta_{t1})\right)\right]$$

but

$$\theta_{t1} = \sin^{-1}\left(\frac{1}{n}\sin(\theta_{i1})\right)$$

so

$$\theta_{t2} = \sin^{-1}\left[n\left(\sin(\theta_{apex})\sqrt{\left(1 - n^{-2}\sin^2(\theta_{i1})\right)} - n^{-1}\cos(\theta_{apex})\sin(\theta_{i1})\right)\right]$$
$$= \sin^{-1}\left[\sin(\theta_{apex})\sqrt{n^2 - \sin^2(\theta_{i1})} - \cos(\theta_{apex})\sin(\theta_{i1})\right]$$

Equation 4.4

This gives us a final expression for the angle of deviation, Equation 4.5. To measure the IoR, three angles will have to be measured; θ_{i1}, θ_{Dev} and θ_{apex}.

$$\theta_{Dev} = \theta_{i1} + \sin^{-1}\left[\sin(\theta_{apex})\sqrt{n^2 - \sin^2(\theta_{i1})} - \cos(\theta_{apex})\sin(\theta_{i1})\right] - \theta_{apex}$$

Equation 4.5 Deviation relation

By taking the derivative can the relation for the minimum deviation angle be determined. In this process is the dependence on the initial angle lost. When solving the system in reverse, we can show that at the angle of minimum deviation the prism configuration has to be symmetric, i.e. $\theta_{i1} = \theta_{t2}$ and $\theta_{t1} = \theta_{i2}$.

$$\frac{\partial\theta_{Dev}}{\partial\theta_{i1}} = 0 = 1 + \frac{\partial\theta_{t2}}{\partial\theta_{i1}} - 0$$

and finally

$$n = \frac{\sin((\theta_{Dev,\min} + \theta_{apex})/2)}{\sin(\theta_{apex}/2)}, \quad n \equiv \frac{n_{material}}{n_{ambient}}$$

Equation 4.6

Section 4.2 Fabry-Pérot interferometry

Interferometry works by the fact that two or more interacting light waves will yield a resulting intensity pattern based on the superposition principle. Constructive interference occurs when the phase difference is an integer number of wavelengths, while destructive interference will occur when the phase difference is an odd integer number of half wavelengths.

The etalon inside a Fabry-Pérot interferometer consists of two thin plates which reflect a part of the light and transmit the rest. A similar effect occurs in a single thicker plane-parallel plate (Figure 4.2). The set-up is similar, but the gap in the middle is now filled with material instead of air or vacuum.

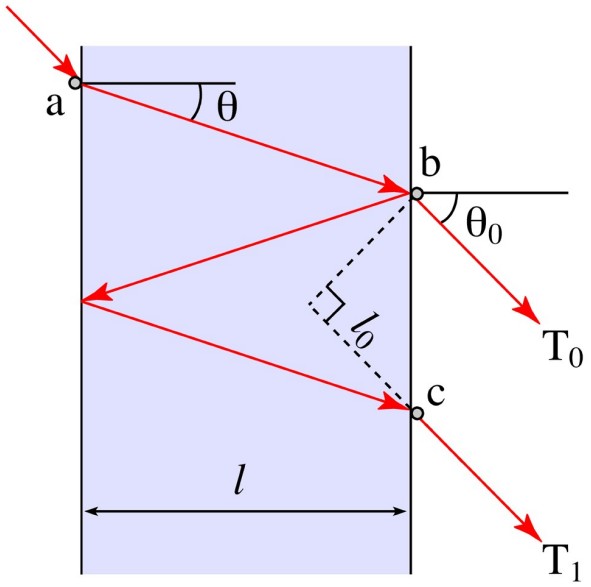

Figure 4.2: schematic overview of the Fabry-Pérot interferometry principle

A light beam enters the plate and propagates to the other boundary. There it is partially reflected back towards the first boundary and partially refracted out of the plate. This effect can go on an infinite number of times. With each interaction with a boundary the intensity of the light is divided between the reflected and refracted light beams. The reflection and transmission coefficients which govern this division differ per material.
The light beams which exits the material, in Figure 4.2 displayed as T_0 and T_1, will give an interference pattern. These beams are parallel to each other. The phase difference between the succeeding transmissions is determined by the optical path length difference and IoR of the etalon material [Wiki], [Be07].
Let's assume an incident light beam with an intensity of unity and a certain phase. The light has a broad spectral range.
Then T_0, the primary exiting light beam, can be parametrized as $T_0 = \tau^2 e^{ikl/\cos(\theta)}$. τ, the transmission coefficient, is present in quadrate since the light has been refracted through the material twice. After every refraction the intensity will have gone down by τ. k is the angular wave number of the light inside the etalon and $l/\cos(\theta)$ is the path length travelled through the material. T_1, the secondary exiting light beam is given by

$$T_1 = \tau^2 \rho^2 e^{2\pi i + \left(\frac{3ikl}{\cos(\theta)}\right) - ik_0 l_0}$$

Equation 4.7

ρ is the reflection coefficient. It comes into the relation now, since the light beam has been reflected twice internally before exiting the material. The two extra phase terms are due to the extra π phase jump at each reflection and the extra path length outside the etalon which the first exiting light beam has travelled. From here on we will forget the phase jump, since it is always a multiple of 2π and as such does not alter the phase.
Every subsequent exiting light beam can be parametrized in the same manner.

$$T_s = \tau^2 \rho^{2s} e^{is\delta}$$

Equation 4.8

δ represents the phase difference between two succeeding exiting beams and is rewritten in Equation 4.9.

$$\delta = \frac{2kl}{\cos(\theta)} - 2k_0 l \tan(\theta)\sin(\theta_0) = 2nk_0 l\cos(\theta) = \frac{4\pi nl}{\lambda_0}\cos(\theta)$$

Equation 4.9 phase difference between two succeeding light beams

The sum of all the light beams exiting the plate leads to the total transmission through the plate. The square of the transmission gives the intensity, Equation 4.10. This equation has a dependence on wavelength through the phase difference δ. Maxima in intensity occur when $\cos(\delta) = 1$, or $\delta = 2m\pi$.

$$I_{tot} = \frac{\tau^4}{1 + \rho^4 - 2\rho^2\cos(\delta)}$$

Equation 4.10 theoretical Fabry-Pérot intensity relation

There are multiple maxima in a Fabry-Pérot interference spectrum; m can be any integer. As can be seen from Equation 4.11 the spacing between sequential fringe maxima is inversely related by the values of the IoR and the thickness of the plate.

$$\frac{4\pi nl}{\lambda_0}\cos(\theta) = 2m\pi$$

$$\frac{2nl}{\lambda_0}\cos(\theta) = m$$

$$k_0' = \frac{m}{2nl\cos(\theta)}$$

Equation 4.11

In the last equation k_0' is no longer the angular wave number, but the 'real' wave number $k \equiv \frac{1}{\lambda}$.

Section 4.3 Calculating the IoR from interference fringes

Rewriting Equation 4.11 one more time leads to Equation 4.12.

$$n(k_m) = \frac{m}{2dk_m}, \quad d = l\cos(\theta)$$

Equation 4.12 IoR Fabry-Pérot relation

The left-hand side of this relation holds the variable we wish to know, while the right-hand side holds several unknowns and/or observables, most notably the fringe order m. The fringe order can, on a correctly sampled spectrum be assumed to change with one every fringe. The initial problem however is finding the absolute fringe order of one fringe from which to start counting.

Following [Bu05], [Gu03], [Ka98] and [Kapc] we have identified several different methods which may yield the fringe order.

Subsection 4.3.1 Solving at three points with the Steepest Descent Method

With three fringe locations k_m a system of equations can be devised which makes the system over determined. Equation 4.11 can be set for all three fringe locations (and their respective IoRs) and similarly also the differences between the outer points with the middle one. This gives us five relations and five unknowns; three IoRs, the thickness and a single fringe order.

Following [Bu05] the Steepest Descent Method was selected to solve this system. The choice for this method was two-fold. The matrix that describes the system is singular; this means that most methods which use the inverse Jacobian of the system are not usable. Secondly, the Steepest Descent Method will also converge for poor initial choices.

Tests have shown that the method will converge to roughly the correct values, but are unable to reach the required accuracy due to some parameters reaching the computer accuracy before that time. This

problem may be solved by gaining a deeper understanding of the Steepest Descent Method and its implementation. In our communication with Dr. Kaplan [Kapc] no mention of this method was made by him.

Subsection 4.3.2 Alternative single wavelength measurements
The minimum deviation refractometry method generates values of the IoR one wavelength per measurement. Let us assume that one or two values of the IoR at the correct temperature are measured with it.
If it is a single measurement, given that the thickness of the sample is known, the fringe order at that wavenumber can be correctly determined. If two measurements are taken, prior knowledge of the thickness of the sample is not even needed. This can also be calculated.

Subsection 4.3.3 reflectance/transmittance
The transmittance and reflectance parameters of Equation 4.10 are also dependent on the IoR. From an accurate measurement of the sample's transmittance the IoR can be roughly calculated.
The transmittance including incoherent addition of multiple reflections can be parametrized by Equation 4.13 [He02]. The parameter τ from Equation 4.10 equals $\sqrt{T}$ and r is the reflectance at a single surface.

$$T = \frac{1 - r}{1 + r}, \quad r = \frac{(n-1)^2}{(n+1)^2}$$
$$K_T \equiv \frac{1 - T}{1 + T}$$
$$n = \frac{1 + \sqrt{K_T}}{1 - \sqrt{K_T}}$$
Equation 4.13

This rough value for the IoR can then be used to constrain the fringe order of the spectrum generated by a very thin plate (spacing between fringe maxima large). With the fringe order constrained, the measured value for the IoR can be improved. This may then again be a starting point for determining the IoR from a thicker sample.
The problem with this method however is that even small errors or variability in the transmission measurements lead to large errors in the IoR value. This makes this method 'tricky' to use.

Subsection 4.3.4 different thicknesses
A transmittance value may give an initial guess for the fringe order with an uncertainty greater than one. A comparison of samples from different thicknesses can be used as a 'vernier scale' to fix the fringe order for both samples. Since both the fringe orders must be integers, by examining two fringes in each sample that are close enough together that the IoR must be negligibly different for the two positions, one can deduce the fringe orders for both samples.
This can be seen from Equation 4.14. The ratio of the fringe orders on the ratios of thickness, fringe maximum location and IoR. If this last ratio can be assumed to be approximately one, the system can be solved.

$$m = 2ndk_0$$
$$\frac{m_1}{m_2} = \frac{d_1 k_1}{d_2 k_2}$$
Equation 4.14

This relation can be done for several positions in both interference spectra. This leads to an even better determination since we also know the absolute fringe difference between the two positions in each spectrum. Despite efforts to implement this method on the spectra we took, we failed to get accurate results. We assume that the spectra did not provide overlapping fringe maxima close enough together.

Subsection 4.3.5 Taylor expansion
Equation 4.11 showed that the spacing between subsequent fringe maxima is dependent on the thickness and the IoR. The thickness is of course not dependent on wavelength. By expanding Equation 4.11 into a Taylor expansion, the fringe order m drops out (Equation 4.15).

$$n(k_1) = n(k_0) + \frac{-m}{2dk_0^2}\Delta k + \frac{m}{2dk_0^3}\Delta k^2 + \frac{-m}{2dk_0^4}\Delta k^3 + \ldots$$

$$\Delta n = n(k_1) - n(k_0) = n(k_0)\sum_{h=1}^{\infty}(-1)^h\left(\frac{\Delta k}{k_0}\right)^h = n(k_0)\left(\frac{1}{1+\frac{\Delta k}{k_0}} - 1\right)$$

$$\frac{\Delta n}{n(k_0)} = \frac{-\Delta k}{k_1}$$

Equation 4.15

A single value of the IoR has to be determined by alternative means. From that starting point the other results can then stepwise be calculated. The drawback of this method is that the errors are locked into an error chain; each calculated IoR values carriers all the errors of the previous steps. Implementation showed that the error propagation is too large to make this method useful.

The only viable option which remains at this time seems to be using an alternative single wavelength measurement. This is unfortunate, since it means we would need a second instrument to determine the IoR with out resorting to literature values. For a large part of the temperature range no literature values are even available.
In the future the Steepest Descent Method should be revisited if we fail to find a viable way of obtaining the single wavelength measurement.

Section 4.4 Error analyses
An important consideration in this design study is an impression of how stringent the constraints are on the variables that influence the IoR. For this reason error analyses were conducted for both methods.

Subsection 4.4.1 Minimum deviation refractometry
All statistical errors in the angles are assumed to be random. The systematic errors are left out is this analysis. As was derived in Section 4.1 there are two sources of uncertainty, the minimum deviation angle and the apex angle.

$$\sigma_n^2 = \left(\frac{\partial n}{\partial \theta_{Dev,\min}}\right)^2 \sigma_{\theta_{Dev,\min}}^2 + \left(\frac{\partial n}{\partial \theta_{apex}}\right)^2 \sigma_{\theta_{apex}}^2$$

Equation 4.16

This leads to an estimate of the uncertainty in the IoR of:

$$\sigma_n^2 = \left(\frac{\cos((\theta_{Dev,\min} + \theta_{apex})/2)}{2\sin(\theta_{apex}/2)}\right)^2 \left(\sigma_{Dev,\min}^2\right) + \left(\frac{\sin(\theta_{Dev,\min}/2)}{2\sin^2(\theta_{apex}/2)}\right)^2 \sigma_{\theta_{apex}}^2$$

Equation 4.17 Uncertainty estimate for the minimum deviation method

In order to achieve accuracies of 10^{-5} or higher, the errors in the angle determinations have to be as good or better. The terms that followed from the derivatives in Equation 4.16 are of order 1 and will not constrain the errors in any significant way. A very detailed error analysis for the minimum deviation method is given in [Te90]. It states that precision measurements (accuracy 10^{-5}) require the errors in the angles to be less than 0.2 arcsec and prism surface flatness of λ/20 or better.

Table 4.1 gives an overview of all sources of potential error that are present in the minimum deviation method or the Fabry-Pérot interferometry method. When a source is not present in the minimum deviation method, the error is stated to be 'not relevant'.
Birefringence can be source of uncertainty for certain materials. When the structure of a material is anisotropic, the IoR can vary according to the polarization of the light. In such a case the IoR found is valid only for that orientation of the material. If the material has a well defined axis of anisotropy, two IoRs can be assigned to the material. This is certainly not the case for every material with significant birefringence.
A prism has a pyramidal error if its faces are not perpendicular to its base plane. This error will add refraction of the light in the vertical direction. The light beam would deviate from the plane defined by source, prism and detector.

Table 4.1: sources of uncertainty and their maximum values

	Maximum errors permissible at relative uncertainty given		
relative uncertainty	10^{-4}	10^{-5}	10^{-6}
apex angle [deg]	2''	0.2''	0.02''
fringe order	*not relevant*	*not relevant*	*not relevant*
Min Dev angle [deg]	2''	0.2''	0.02''
incident angle [deg]	*not relevant*	*not relevant*	*not relevant*
Intrinsic birefringence	10^{-4}	10^{-5}	10^{-6}
lack of flatness [deg]	0.4''	0.04''	0.004''
pyramidal error [deg]	2''	0.2''	0.02''
Thickness	*not relevant*	*not relevant*	*not relevant*
Resolution	*not relevant*	*not relevant*	*not relevant*
temperature [K]	1	0.1	0.01

Subsection 4.4.2 Fabry-Pérot interferometry
In Equation 4.12 we see four potential sources of statistical error, thickness, fringe maxima location, incident angle and temperature. These errors are all expected to be random. The fringe order must always be known exactly.

$$\sigma_n^2 = \left(\frac{\partial n}{\partial l}\right)^2 \sigma_l^2 + \left(\frac{\partial n}{\partial k_0}\right)^2 \sigma_{k_0}^2 + \left(\frac{\partial n}{\partial \theta}\right)^2 \sigma_\theta^2 + \left(\frac{\partial n}{\partial T}\right)^2 \sigma_T^2$$

Equation 4.18 Uncertainty estimate for the Fabry-Pérot method

The individual derivative terms can be rearranged to very simple relations. In Equation 4.18 we see that the first three terms are all linearly dependent on the IoR. The fourth derivative we cannot parametrize as was explained in Chapter 2.

$$\left(\frac{\partial n}{\partial l}\right) = \frac{m}{2k_0\cos(\theta)}\frac{1}{l^2} = \frac{n}{l}$$
$$\left(\frac{\partial n}{\partial k_0}\right) = \frac{m}{2l\cos(\theta)}\frac{1}{k_0^2} = \frac{n}{k_0}$$
$$\left(\frac{\partial n}{\partial \theta}\right) = \frac{m}{2lk_0}\frac{\sin(\theta)}{\cos^2(\theta)} = n\tan(\theta)$$
$$\left(\frac{\partial n}{\partial T}\right) = ?$$

Equation 4.19

The relative uncertainty estimate shows that these have a one-on-one relation for the thickness and fringe maxima locations. The incident angle error is multiplied by tan(θ). tan(θ) is significantly smaller

than 1 for small angles. The expression $\frac{\partial n}{\partial T}$ is again the thermo-optic coefficient. Its value is of order 10^{-4} or smaller.

$$\left(\frac{\sigma_n}{n}\right)^2 = \left(\frac{\sigma_l}{l}\right)^2 + \left(\frac{\sigma_{k_0}}{k_0}\right)^2 + \left(\sigma_\theta \tan(\theta)\right)^2 + \left(\frac{1}{n}\frac{\partial n}{\partial T}\right)^2 \sigma_T^2$$

Equation 4.20 Relative uncertainty estimate Fabry-Pérot method

Table 4.2 again gives an overview of all sources of potential error that are present in the minimum deviation method or the Fabry-Pérot interferometry method. Now when a source is not present in the Fabry-Pérot interferometry method, the error is stated to be 'not relevant'.
Ideally the front and back boundaries of the plane sample are perfectly parallel to each other. Any deviation in this parallel-ness will add to the error in the angle.

Table 4.2: sources of uncertainty and their maximum values

	Maximum errors permissible at relative uncertainty given		
relative uncertainty	10^{-4}	10^{-5}	10^{-6}
apex angle [deg]	*not relevant*	*not relevant*	*not relevant*
fringe order	0	0	0
Min Dev angle [deg]	*not relevant*	*not relevant*	*not relevant*
incident angle [deg]	0.1	0.03	0.01
intrinsic birefringence	10^{-4}	10^{-5}	10^{-6}
plane parallel-ness [deg]	0.1*n	0.03*n	0.01*n
pyramidal error [deg]	*not relevant*	*not relevant*	*not relevant*
thickness	10^{-4}	10^{-5}	10^{-6}
Spectral resolution[1] [cm^{-1}]	$4*10^{-2}$	$4*10^{-3}$	$4*10^{-4}$
Temperature[2] [K]	0.5	$5*10^{-2}$	$5*10^{-3}$

Section 4.5 Discussion
As we read in the Chapter 3 all groups we found are working with some form of the minimum deviation method. This method has been well established and has been demonstrated to work also at cryogenic temperatures. But most of the equipment for the Fabry-Pérot interferometry method is available at ASTRON.

There are even more persuasive arguments for the interferometry method. The minimum deviation method uses discrete wavelengths, while we can cover a wide wavelength range in a single measurement. There are no moving parts, which is always a difficulty in a cryogenic environment. The error analysis also doesn't show any impossible constraints on the parameters which have to be achieved. The only problem is finding a single fringe order.

At this stage of the feasibility study we have decided to further investigate the development of a refraction measuring device based on the Fabry-Pérot interferometry approach. In the next chapter we will first describe a new method we have developed. This method should provide us with the single alternative IoR measurements needed to constrain the fringe order.

[1] Resolution is given for the minimal wavenumber in our range, i.e. 400 cm^{-1} (25μm).

[2] Given an estimate of $2*10^{-4}$ for the thermo-optical coefficient and refractive index of 2, the temperature error must be smaller than 1K. However because these are estimations a maximum temperature error of 0.5K is proposed at an accuracy of 10^{-4}.

Chapter 5: IoR Measurement method, keeping wavelength constant

In Section 4.3 we discussed methods to obtain the single fringe order needed to constrain our system of fringe maxima obtained through Fabry-Pérot interferometry. We concluded that the most viable option at this time was obtaining the IoR at a single wavelength by alternative means.

We are investigating the dependency of the IoR on two variables, the wavelength and the temperature. The Fabry-Pérot method was designed to measure the IoR behaviour over wavelength, while keeping the temperature constant. The method we will describe next will be the other way around. We will measure the IoR behaviour over temperature, while keeping the wavelength constant.

Section 5.1 Classic interferometry

The optical path length (OPL) is the product of the geometric length of the path that light follows through a system and the IoR of the medium through which it propagates. A phase difference is created between two light rays when one ray travels through a medium, while the other travels through a vacuum. This fact forms the basis for the following method.

At ASTRON we have a Wyko interferometer with a beam diameter of 6 inch and a HeNe laser (wavelength of λ_0 = 632.816 nm). We will measure the fringe patterns that are created by plane-parallel samples of which half their front plane is coated to be a 100% reflective and the other half is left transparent. The sample's back plane will be placed on a mirror.

Two phase deviations, with respect to the reflective background, can now be distinguished. These deviations will change with temperature.

Where the sample is a 100% reflective, the OPL will be decreased by twice the length of the sample. Until now we have not expressly mentioned it, but the thickness of the sample is also dependent on temperature. Accurate knowledge of the thickness at all investigated temperatures is therefore a must, also for the Fabry-Pérot method.

Where the sample is transparent, the OPL will be altered due to the IoR and the length of the sample.

The interferometer can compare these OPLs against a reference OPL. The resultant optical path difference (OPD) is observed through the resultant phase difference. Any multiples of 2π in the OPD won't add to the phase difference and cannot be detected.

The workings of the interferometer are further depicted in the next figure.

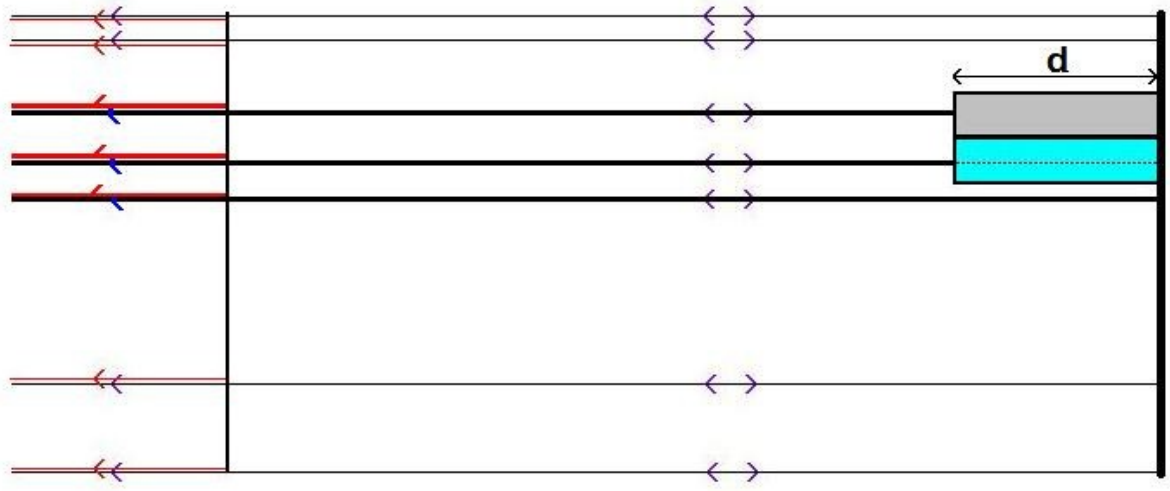

Figure 5.1 Schematic overview of the Wyko interferometer

As is depicted in Figure 5.1, the Wyko interferometer emits a beam of parallel light rays. This light is immediately split into two beams, a reference beam (depicted going to the left) and the 'work' beam (to the right). The work beam is reflected back at the mirror and samples. At the detector the two beams are again combined to form an interferogram; an image of the phase deviation between the two beams.

We will derive the equations which govern the phase deviations and show how we can determine the IoR and CTE with this method.

The phase deviation for the part of the sample which is reflectively coated is linearly related to twice the combined lengths of the sample, d, and its coating, d_c. The phase is given as a ratio to the laser

wavelength, Equation 5.1. Equation 5.2 gives the derivative of this relation with respect to temperature.

$$\phi = \frac{-2}{\lambda_0}\left(d(T) + d_c(T)\right)$$

Equation 5.1 phase deviation from the coated sample

$$\frac{d\phi}{dT} = \frac{-2}{\lambda_0}\frac{\partial\left(d + d_c\right)}{\partial T} = \frac{-2}{\lambda_0}\left(\frac{\partial d}{\partial T} + \frac{\partial d_c}{\partial T}\right)$$

Equation 5.2 change in phase deviation over temperature

The total change in phase deviation we will observe is parametrized in Equation 5.3.

$$\Delta\phi = \int \frac{d\phi}{dT}dT = \frac{-2}{\lambda_0}\int\left(\frac{\partial d}{\partial T} + \frac{\partial d_c}{\partial T}\right)dT$$

$$d = d_0 + d_0\int CTE dT; \quad \frac{\partial d}{\partial T} = d_0 CTE$$

$$\Delta\phi = \frac{-2}{\lambda_0}\int\left(d_0 CTE + d_c CTE_c\right)dT$$

Equation 5.3

As a last step, we assume the CTE to change only a very little over a small change in temperature. The integration 'subject' can be assumed constant and the integral reduces to ΔT. This leads to Equation 5.4.

$$\frac{\Delta\phi}{\Delta T} = \frac{-2}{\lambda_0}\left[d_0 CTE + d_c CTE_c\right]$$

Equation 5.4

Equation 5.4 has two unknowns, the CTE and the combined term $d_c CTE_c$. Using a minimum of two samples, which are uniformly coated and have had their initial thickness measured, will be enough to find a unique solution for these unknowns. d_0 is the thickness of the samples at the lower integration limit.

The transparent part of the sample will show a different phase deviation. The OPL of the light now changes because it travels through the sample instead of vacuum. We see this in Equation 5.5. The phase deviation can be split into two parts; -d(T) and d(T)n(T). This first part is the OPL we have to subtract and the second part is the OPL we have to replace it with. Equation 5.6 is the derivation of this relation with respect to temperature.

$$\phi = \frac{2}{\lambda_0}d(T)\left(n(T) - 1\right)$$

Equation 5.5 phase deviation from the transparent sample

$$\frac{d\phi}{dT} = \frac{2}{\lambda_0}\left(\frac{\partial}{\partial T}(dn) - \frac{\partial d}{\partial T}\right)$$

Equation 5.6 change in phase deviation over temperature

The change in phase deviation can be found in a similar way to Equations 5.3 and 5.4.

$$\Delta\phi = \int \frac{d\phi}{dT} dT = \frac{2}{\lambda_0} \int \left(\frac{\partial dn}{\partial T} - \frac{\partial d}{\partial T} \right) dT$$

$$\Delta\phi = \frac{2}{\lambda_0} \int \left(d_0 CTE(n-1) + n_0 d \frac{dn}{dT} \right) dT$$

Equation 5.7

$$\frac{\Delta\phi}{\Delta T} = \frac{2}{\lambda_0} \left[d_0 CTE(n-1) + n_0 d \frac{dn}{dT} \right]$$

Equation 5.8

Equation 5.8 has a single unknown. The CTE and subsequently the thickness d can be found from Equation 5.4. The only unknown is the IoR. It is present in this relation in two forms, n_0 and $\frac{dn}{dT}$.

The d_0 and n_0 are the thickness and the IoR value as valid at the lower integration limit, and d and n at the higher integration limit.

All these changes in phase deviations will give us the IoR and CTE over a complete temperature range and thus providing the input we need for the Fabry-Pérot method.

Section 5.2 Error analysis

The changes in phase deviations will be very small. Looking at Equations 5.4 and 5.8, we estimate that $\frac{\Delta\phi}{\Delta T}$ will be at the most of order 10^{-1} and most likely much smaller. Such small values will place heavy constraints on our system. The following error analysis will show that the tolerances are within obtainable limits. This analysis focuses on the statistical errors, not on any systematic errors.

In Section 5.1 we showed that we can find a solution for the CTE by measuring the phase deviation of two samples of different height. By rewriting Equation 5.4 to Equation 5.10, we see how this can be done. Our assumption was that the coating is equal for both samples. In that case will Equation 5.9 yield the same answer for both samples and result in Equation 5.10.

$$d_c CTE_c = \frac{-\lambda_0}{2} M - d_0 CTE, \qquad M \equiv \left(\frac{\Delta\phi}{\Delta T} \right)$$

Equation 5.9

$$CTE = \frac{-\lambda_0}{2} \frac{M_2 - M_1}{d_{0.2} - d_{0.1}}$$

Equation 5.10

Equation 5.11 shows the relative uncertainty for our CTE value. It is clear from this relation that the strictest tolerance will be on the determination of the change in phase deviation M. The error in the thickness is softened by its ratio to thickness. As was just stated, M will be at the most of order 10^{-1} and as such increase the relative uncertainty.

$$\frac{\sigma_{CTE}^2}{CTE^2} = \frac{\lambda_0^2}{8} \left(\left(\frac{\sigma_M}{M_2 - M_1} \right)^2 + \left(\frac{\sigma_{d_0}}{d_{0,2} - d_{0,1}} \right)^2 \right)$$

Equation 5.11 Relative uncertainty estimate CTE

From the uncoated samples we can derive the thermal-optical coefficient $\frac{dn}{dT}$. The uncertainty in the TOC will depend on errors in the other variables from Equation 5.8. Rewriting Equation 5.8 into Equation 5.12, we can derive an uncertainty estimate for our TOC value.

$$\frac{dn}{dT} = \frac{\frac{\lambda_0}{2}M + d_0 CTE(1 - n_0)}{n_0 d_0(1 + 2CTE\Delta T)}$$

Equation 5.12

Equation 5.13 gives the uncertainty in our TOC value. The expression (1+2CTE∆T) we find in each term is approximately 1. The nominators of each term are also all of order 1 or smaller. The main parameters in each term which drive the strictness of each error are the thickness and IoR. For the errors due to the change in phase deviation, thickness, IoR and temperature this means the effects of the individual errors are softened. The error due to the CTE is driven by the expression $\frac{1 - n_0}{n_0}$, which is of order 1.

$$\begin{aligned}
\sigma^2_{\frac{dn}{dT}} = & \left(\frac{\lambda_0}{2n_0 d_0(1 + 2CTE\Delta T)}\right)^2 \sigma^2_M + \left(\frac{-\frac{\lambda_0}{2}M}{\left(n_0 d_0^2(1 + 2CTE\Delta T)\right)}\right)^2 \sigma^2_{d_0} \\
& + \left(\frac{(2n_0 - 1)d_0 CTE - \frac{\lambda_0}{2}M}{n_0^2 d_0(1 + 2CTE\Delta T)}\right)^2 \sigma^2_{n_0} \\
& + \left(\frac{1 - n_0}{n_0} - \frac{\lambda_0 M\Delta T}{n_0 d_0(1 + 2CTE\Delta T)^2}\right)^2 \sigma^2_{CTE} \\
& + \left(\frac{-\left(\frac{\lambda_0}{2}M + d_0 CTE(1 - n_0)\right)2CTE}{n_0 d_0(1 + 2CTE\Delta T)^2}\right)^2 \sigma^2_{\Delta T}
\end{aligned}$$

Equation 5.13 Uncertainty estimate TOC

Our overall objective is determining the IoR to an accuracy of 10^{-5}. To make sure we have this accuracy at the spectrometer, here at the interferometer we wish to obtain an accuracy of 10^{-6}. This same argument also applies to the accuracy wanted for the thickness.
As can be seen from Equations 5.14 and 5.15, the relative errors in the thickness and IoR are related to the errors in the CTE, TOC and temperature.

$$\begin{aligned}
d &= d_0(1 + CTE\Delta T) \\
\sigma^2_d &= (1 + CTE\Delta T)^2 \sigma^2_{d_0} + (d_0\Delta T)^2 \sigma^2_{CTE} + (d_0 CTE)^2 \sigma^2_T \\
\frac{\sigma^2_d}{d^2} &\cong \frac{\sigma^2_{d_0}}{d_0^2} + \Delta T^2 CTE^2\left(\frac{\sigma_{CTE}}{CTE}\right)^2 + \Delta T^2 CTE^2\left(\frac{\sigma_T}{\Delta T}\right)^2
\end{aligned}$$

Equation 5.14

$$n = n_0\left(1 + \frac{dn}{dT}\Delta T\right)$$

$$\sigma_n^2 = \left(1 + \frac{dn}{dT}\Delta T\right)^2 \sigma_{n_0}^2 + \left(n_0 \Delta T\right)^2 \sigma_{\frac{dn}{dT}}^2 + \left(n_0 \frac{dn}{dT}\right)^2 \sigma_T^2$$

$$\frac{\sigma_n^2}{n^2} \cong \frac{\sigma_{n_0}^2}{n_0^2} + \left(\Delta T \frac{dn}{dT}\right)^2 \left(\frac{\sigma_{\frac{dn}{dT}}}{\frac{dn}{dT}}\right)^2 + \left(\Delta T \frac{dn}{dT}\right)^2 \left(\frac{\sigma_T}{\Delta T}\right)^2$$

Equation 5.15

Table 5.1 shows the maximum errors permissible to obtain the tolerances wanted in the IoR and thickness. For clarity are only the direct variables as found in the above uncertainty relations shown in Table 5.1. Tables 5.2 and 5.3 further specify the tolerances on the observables from the constraints imposed on the TOC and CTE respectively from the error analysis in this section.

Table 5.1 sources of uncertainty and their maximum relative errors permissible for the IoR and thickness (combined table)

	Maximum errors permissible at relative uncertainty given		
Relative uncertainty	10^{-4}	10^{-5}	10^{-6}
thickness	10^{-4}	10^{-5}	10^{-6}
IoR	10^{-4}	10^{-5}	10^{-6}
CTE	10^{1}	10^{0}	10^{-1}
TOC	10^{0}	10^{-1}	10^{-2}
Temperature[3]	10^{0}	10^{-1}	10^{-2}

The values given in Table 5.2 can be checked against Equation 5.13. There we derived the error relation between the mentioned parameter and the thermo-optic coefficient. Similarly, one can check the tolerances of Table 5.3 be against Equation 5.11.

Table 5.2 sources of uncertainty and their maximum values for TOC

	Maximum errors permissible at relative uncertainty given		
Relative uncertainty	10^{0}	10^{-1}	10^{-2}
Phase difference M (absolute error)	10^{1}	10^{0}	10^{-1}
Phase angle (absolute error)	10^{0}	10^{-1}	10^{-2}
Temperature [K] (absolute error)	10^{2}	10^{1}	10^{0}
Thickness d_0 [µm] (relative error)	10^{1}	10^{0}	10^{-1}
Refractive index n_0 (much stricter above)	10^{-1}	10^{0}	10^{-1}
CTE (relative error)	10^{1}	10^{0}	10^{-1}

[3] The maximum temperature error for the IoR is shown here. The temperature error for the thickness is one order less strict, but for obvious reasons we have given the stricter tolerance here.

Table 5.3 sources of uncertainty and their maximum values for CTE

	Maximum errors permissible at relative uncertainty given		
Relative uncertainty	10^{1}	10^{0}	10^{-1}
Phase angle (absolute error)	10^{-1}	10^{-2}	10^{-3}
Temperature [K] (absolute error)	10^{1}	10^{0}	10^{-1}
Thickness d_0 [µm] (relative error)	10^{2}	10^{3}	10^{4}

Section 5.3 Losing unwanted reflections

In our analysis above we have not taken into account the effect of multiple kinds of reflection in the optically transparent samples. In total there are three kinds of reflections possible from the sample. Both the front and back planes of the sample will reflect light. Further, plane-parallel samples will generate internal fringes. This is the effect we use with the Fabry-Pérot interferometry method. Here our interests lie solely with the reflections from the back plane.

Reflections from the front plane can be suppressed by coating the samples with an anti-reflective coating. To suppress the detection of internal fringing a wedge should be introduced into every sample [Je91]. By introducing the wedge the internal reflections will be angled away from the detector. Introducing a wedge is difficult however. A wedge will also angle the wanted reflection away slightly. Therefore can the value of the wedge be no larger than the tolerance on the thickness.

Chapter 6: IoR measurements using the Fabry-Pérot interferometry method
In Chapter 4 we have derived the relation (Equation 4.10) we expect to observe in our measurements. In this chapter we will present measurements we have collected and compare them to the theory.

Spectra have been taken with the Varian 7000/7000e FT-IR spectrometer which ASTRON owns. Two etalon samples have been made from silicon. These samples do not meet the tolerances as set out in Table 4.2, but are good enough to do test measurements.
The uncertainty in the thickness in Table 6.1 is an absolute uncertainty. The parallelism value expresses the variation in thickness as measured along the edges of each sample.

Table 6.1 characteristics of the silicon samples

Sample	thickness	diameter	Clear aperture	Parallelism
#1	1.5mm ± 7µm	1 inch	20mm	1µm
#2	2.5mm ± 10µm	1 inch	20mm	1µm

Using these samples a few initial measurements were done at 27°C. This temperature was chosen, because for silicon at this temperature the Sellmeier function has been derived [Gh98].

Section 6.1 Measurement set-up
The samples were placed in a custom designed holder and positioned within the internal measurement compartment of the spectrometer. To the holder was attached a PID controlled heating system with a two-wire RTD sensor.
The following hardware settings were set on the spectrometer.

Setting NIR2
- Detector DTGS
- Light source NIR source
- Beam splitter NIR-Quartz
- Aperture 1 cm^{-1}
- Resolution 0.25 cm^{-1}
- Wavenumber range 2800-8000 cm^{-1}

Setting MIR1
- Detector DTGS
- Light source Ceramic source (MIR)
- Beam splitter KBr
- Aperture 0.25 cm^{-1}
- Resolution 0.25 cm^{-1}
- Wavenumber range 400-6000 cm^{-1}

We also chose certain specific software settings in the control software of the spectrometer. In de 'compute' menu before taken a spectrum, check the apodization option 'NB medium' with zero filling at 16. This will ensure a computationally higher resolution (16x) and a smooth spectrum, which is the Varian recommended setting for all spectra. NB stands for the Norton-Beer apodization function.
The observed spectra were read into MATLAB were the fringe separation was determined with *truepeaks2.m*. This self-written algorithm first fits a piece-wise spline with high resolution (0.001 cm^{-1}) to the data points of the spectrum and then finds the location of the fringe maxima. By fitting a spline to the spectrum the spectral resolution is improved beyond the resolution of the spectrometer. This procedure will not introduce phantom fringe maxima, since the hardware resolution is high enough to sample between adjacent fringe maxima.

A set of comparative IoR values was computed from the Sellmeier relation for silicon at the appropriate wavelength range, Table 6.2 [Gh98]. A wavelength resolution of $\Delta\lambda = 10^{-6}$ µm was taken to overmatch the resolution of the observed spectra. The resultant IoR vector was then entered into the Fabry-Pérot intensity relation, Equation 4.10. With this equation a comparative spectrum was generated and its fringe maxima were located.

Table 6.2 Sellmeier coefficients for silicon at 27°C and between wavelengths 1.36 µm and 11 µm

C_1	B_1	B_2	λ_1 [µm]	λ_2 [µm]
3.12896495	8.54278728	0.00527631	0.11337073	1500

Section 6.2 Measurements

By comparing our observed spectra to the predictions from the Sellmeier relation the validity and accuracy of our measurements can be demonstrated.

A first indication of the accuracy of our measurements can be made from plotting the distance between adjacent fringe maxima in the spectrum, Figure 6.1. This figure shows the fringe separation we have predicted (red) and the fringe separation we observe in our spectra (blue and green). As can be seen, the fringe separation of our measurements follows the curve of the prediction very well. The measurements only show more spread. The panel on the left is from sample #1, the panel on the right from sample #2. The dependence of the fringe spacing value on thickness (Equation 4.11) can also be seen here. Sample #1, which is thinner, has larger fringe spacing than sample #2.

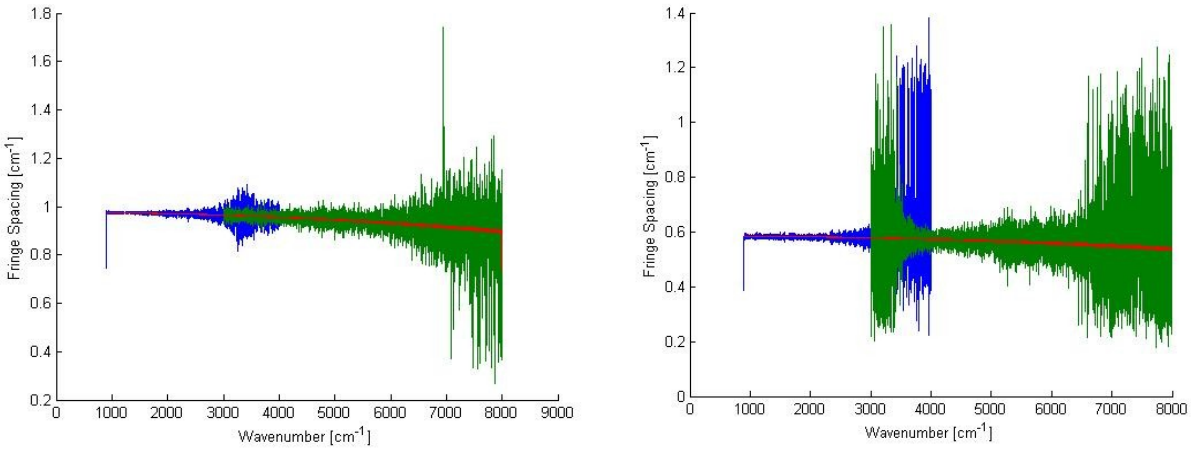

Figure 6.1 Predicted (red) vs. observationally determined (blue and green) fringe separation for both samples at 27°C.

We see an increase in spread at the higher wave numbers. We theorize that this is due to light profiles of the spectrometer light source. The source can be approximated by a black body source. At the shorter wavelengths we enter the exponential cut-off region of the black body spectrum. Gaussian noise, via the background calibration, will play a greater role here.

In the image from sample #2 we also see an increased spread at the NIR2 setting (green) at the lower wave number side. The source of this spread is related to the NB apodization function. At the lower wave number side we are also dealing with a decline of light strength, though less suddenly than on the higher wave number side. The random noise addition from the background again leads to small fluctuations in the spectrum which the apodization function transforms into false peaks. Given that the region affected is also covered by the MIR1 spectrum, we have not taken further action to suppress the noise.

Section 6.3 The IoR calculated

To calculate the IoR over the entire wavelength range we arbitrarily selected a single IoR value from the Sellmeier relation. At a later stage when we have our own method of obtaining this value, that one will of course will have our preference.

As can be seen from the top panels of Figures 6.2 through 6.5 good comparison is seen between the IoR values we derived (blue) and the predicted outcome (green). A third line is drawn in the top panels. This line belongs to another set of measurements (also in [Gh98]). It is added to show the difference between the two available comparisons we have. That difference is at the 3rd decimal. This indicates that there is still an uncertainty of the measured value of this well characterized material at the 3rd decimal. We have chosen for a comparison with the Sellmeier coefficients above these other observations for several reasons. First of all, the derivation of the Sellmeier coefficients is based on observations, but has been augmented with further knowledge about the solid state characteristics of the material. Secondly, the other set is based on several unconnected, mostly older, measurements.

The bottom panels show the deviation between the prediction and our calculation. Several things draw our attention here.

First, the overall deviation is of order 10^{-4}, an order too large for our goal. However, we can explain it. One might first recall that the uncertainty in the thicknesses of the samples is an order too large. However, this we have corrected for by selecting a second IoR from our prediction. With the method described in Subsection 4.3.2, we are no longer constrained by the thickness uncertainty.

But, we have only roughly positioned the sample perpendicular to the light in the measurement chamber. Also, the light beam produced by the spectrometer is convergent inside the measurement chamber. This introduces a set of angles deviating from perpendicular. These two errors in the incident angle are an error source of the order 10^{-4}.
The second thing to draw our attention is the shape of the deviation. Our prediction is drawn from the Sellmeier relation, which is a smooth curve. It cannot parametrize small variations like our measurements can. The distinctive 'jump' at 9 μm for instance is probably due to a real intrinsic characteristic of silicon. Unfortunately, in the course of this project, we have not done further measurements with other materials. We feel this is a missed opportunity, which would have shed more light onto this matter.
Thirdly, we notice the change in shape between Figures 6.4 and 6.5, which is especially noticeable at the edges. As we will see below, these shapes are seen at multiple measurements. They seem to be connected to the individual samples and their positioning in the measurement chamber.

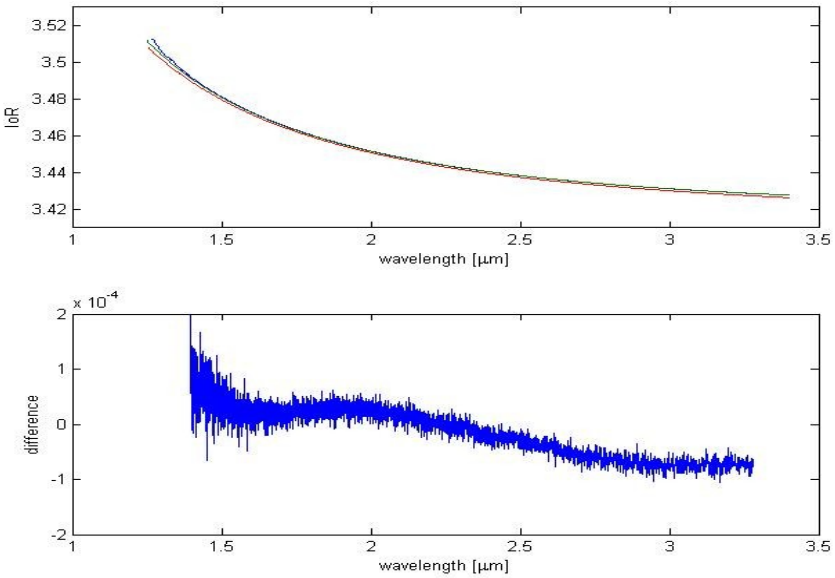

Figure 6.2 Theoretical vs. Calculated IoR with their difference. Results for 1.5mm sample and NIR2 settings

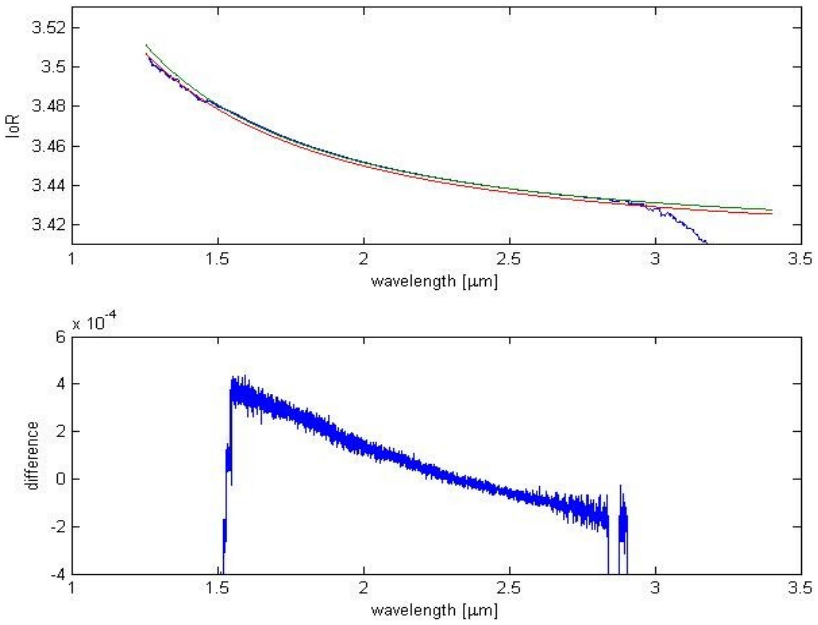

Figure 6.3 Theoretical vs. Calculated IoR with their difference. Results for 2.5mm sample and NIR2 settings

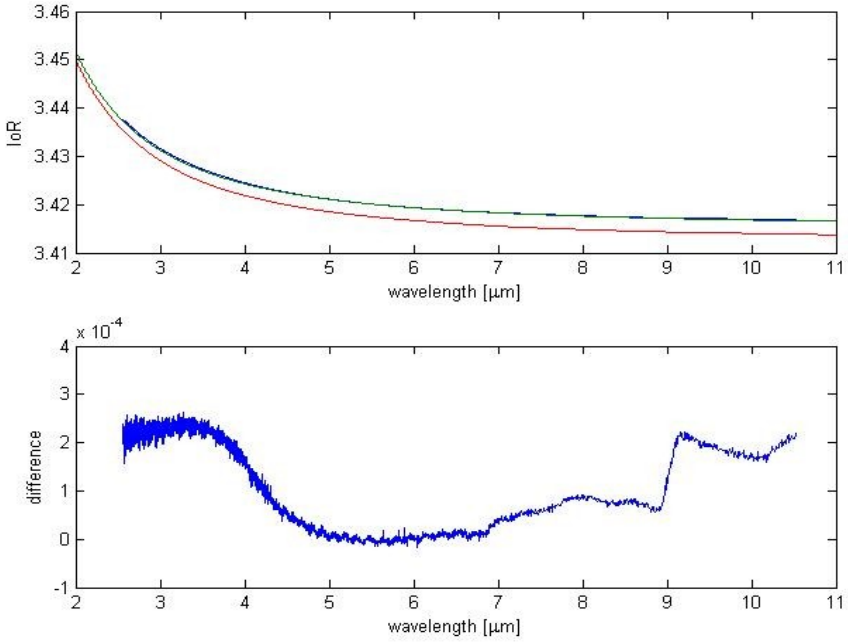

Figure 6.4 Theoretical vs. Calculated IoR with their difference. Results for 1.5mm sample and MIR1 settings

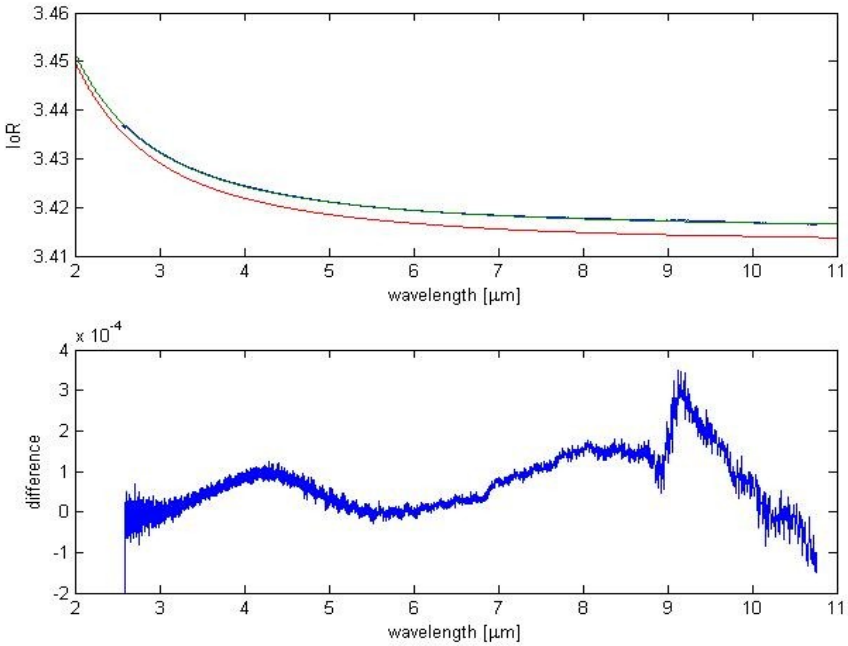

Figure 6.5 Theoretical vs. Calculated IoR with their difference. Results for 2.5mm sample and MIR1 settings

Another aspect of the quality assurance of the measurement method is the reproducibility with which we can repeat the measurements. Results are shown in Figure 6.6. We analyze the repeatability by plotting the deviations for different, subsequent, measurements preformed with the Varian spectrometer. We see that both the accuracy and the reproducibility are at 10^{-4}. All four figures show a point through which all deviations are plotted. This is the point at which we have selected the IoR from the Sellmeier relation.

The spread in the slope of the deviations is due to the small off-sets in the locations of the fringe locations. This results in the assignment of the same fringe number to slightly different locations. That leads to slightly different vectors. This variation may be deminished by adding more scans into a single spectrum. Currently the spectrometer is set to add 16 scans.

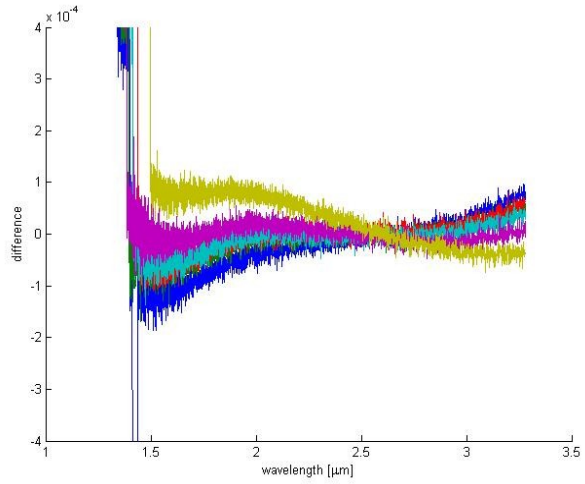

Figure 6.6a Accuracy of the Varian spectrometer. Shown are several subsequent measurements of the #1 sample at the NIR2 setting

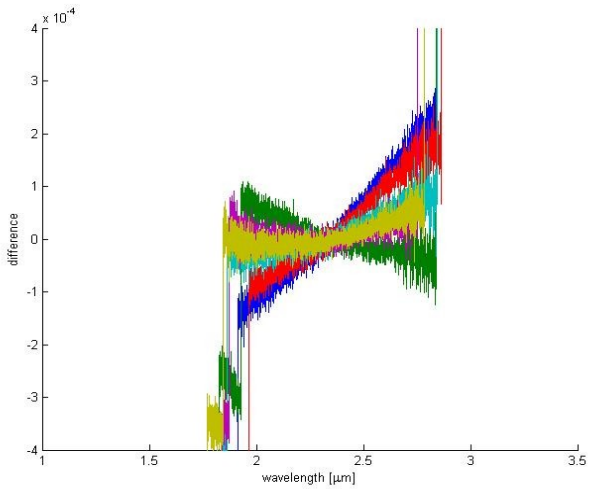

Figure 6.6b Accuracy of the Varian spectrometer. Shown are several subsequent measurements of the #2 sample at the NIR2 setting

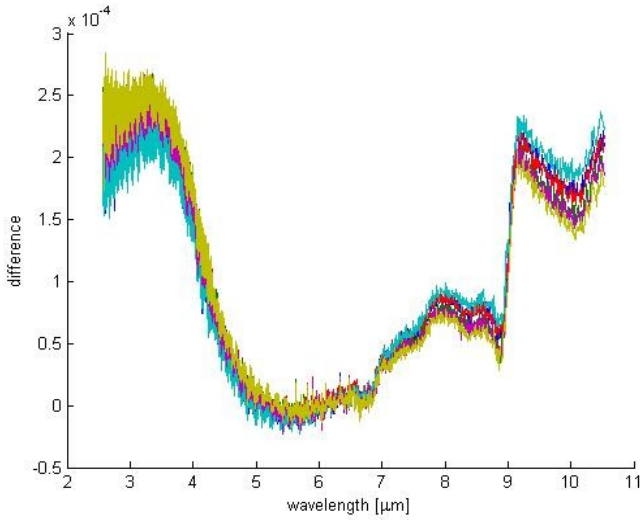

Figure 6.6c Accuracy of the Varian spectrometer. Shown are several subsequent measurements of the #1 sample at the MIR1 setting

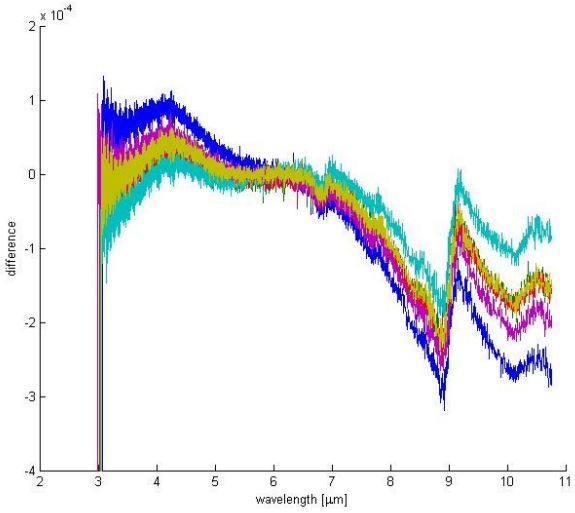

Figure 6.6d Accuracy of the Varian spectrometer. Shown are several subsequent measurements of the #2 sample at the MIR1 setting

Chapter 7: IoR measurements using the interferometer set-up

Five samples have been made from BK7 material. Our first objective is to get a good understanding of the system and all its sources of environmental error. BK7 was chosen, because it was available at ASTRON, is transparent at 632nm (unlike silicon) and is included in [Gh98].
These samples have been coated with 100% reflective coating for half their top planes. No AR coating was applied to the other half, nor was a wedge included at this time.

Table 7.1 characteristics of the BK7 samples

Sample	Thickness	Clear aperture	flatness	parallelism
#1	11.922mm ± 2µm	16mm	< ½ fringe	2µm
#2	16.452mm ± 2µm	16mm	< ½ fringe	2µm
#3	20.771mm ± 1µm	16mm	< ½ fringe	< 1µm
#4	24.867mm ± 1µm	16mm	± ½ fringe	1µm
#5	29.467mm ± 1µm	16mm	± ½ fringe	1µm

Section 7.1 Measurement set-up

ASTRON provides the Wyko interferometer with a 6 inch beam diameter and HeNe laser. The set-up is depicted in Figure 7.1. The two mirrors, the one under the samples and the top one, are both made from Zerodur material. This material was chosen because it has a very low CTE value.
The holder underneath is made from aluminum and has heaters placed on its underside and the tip-tilt mechanism has been bolted to the optical table. The wires one can see in the bottom left corner are connected to the PID thermal controller.

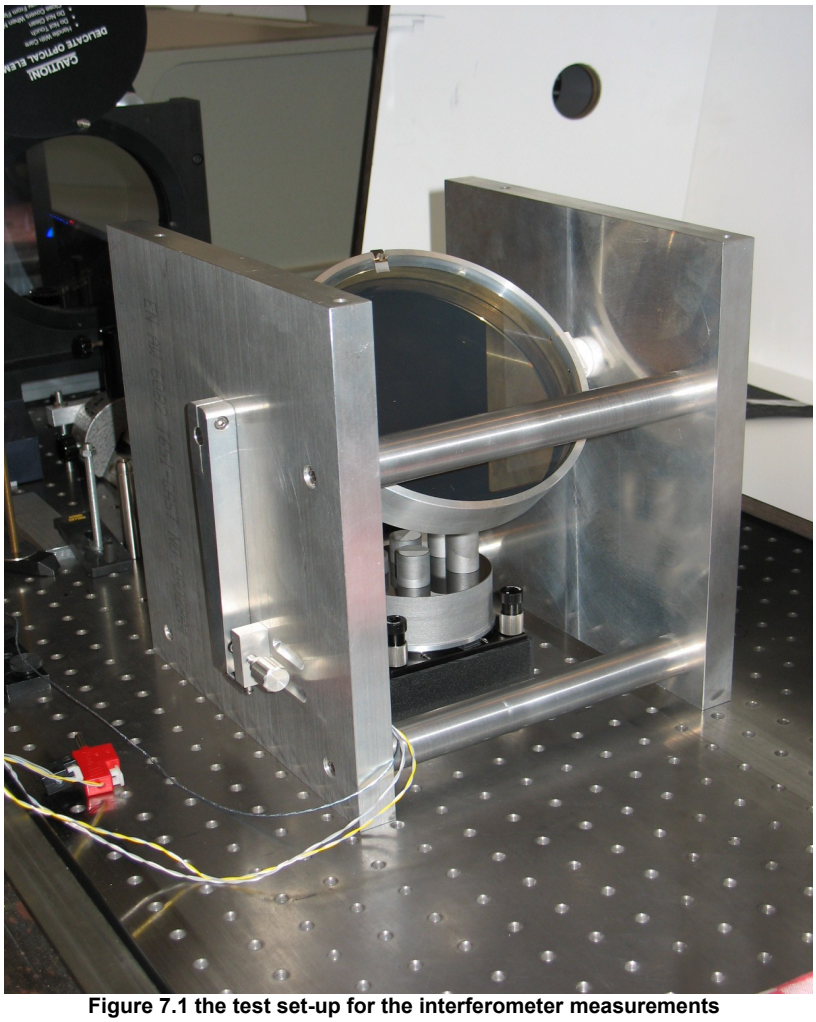

Figure 7.1 the test set-up for the interferometer measurements

The whole system is aligned in two stages. First the overall image is found by positioning the top mirror. Then with the tip-tilt rotators on the holder the precision alignment was made.
Interferograms were taken with the IntelliWave software. For some of the following tests that are described this process was automated. This allowed us to take multiple measurements at set time intervals.

Section 7.2 Measurements

Subsection 7.2.1 turbulence

Our first tests were designed to see to what extend our set-up suffers from turbulence. The whole system of holder, mirror and samples was step-wise heated to 30°C with a PID controlled heating system.
The room temperature is around 21°C. When the set-up was heated to 30°C, the temperature difference resulted in significant, visible turbulence. For the lower temperature differences, turbulence was not visible.
This turbulence has two main sources. First the hot air which is formed under the holder close to the heaters. The hot air leaves this pocket and travels upwards along the edges of the holder. This created eddies in the images along the outer edges of the samples. Second, after some time the mirror will have warmed, creating turbulence on the whole mirror.
There is of course one 'simple' option to get rid of turbulence, vacuum. This option will be discussed further in section 8.2.

Subsection 7.2.2 thermal heating

More detailed testing was then done to investigate the thermal response of the overall system. Figure 7.2 shows the thermal response at three points; the tops of the base mirror, the smallest sample (#1) and the largest sample (#5). The two spikes visible in the left hand side of the figure as due to unintentional temperature spikes in the software of the heaters. This problem was solved during the measurements.

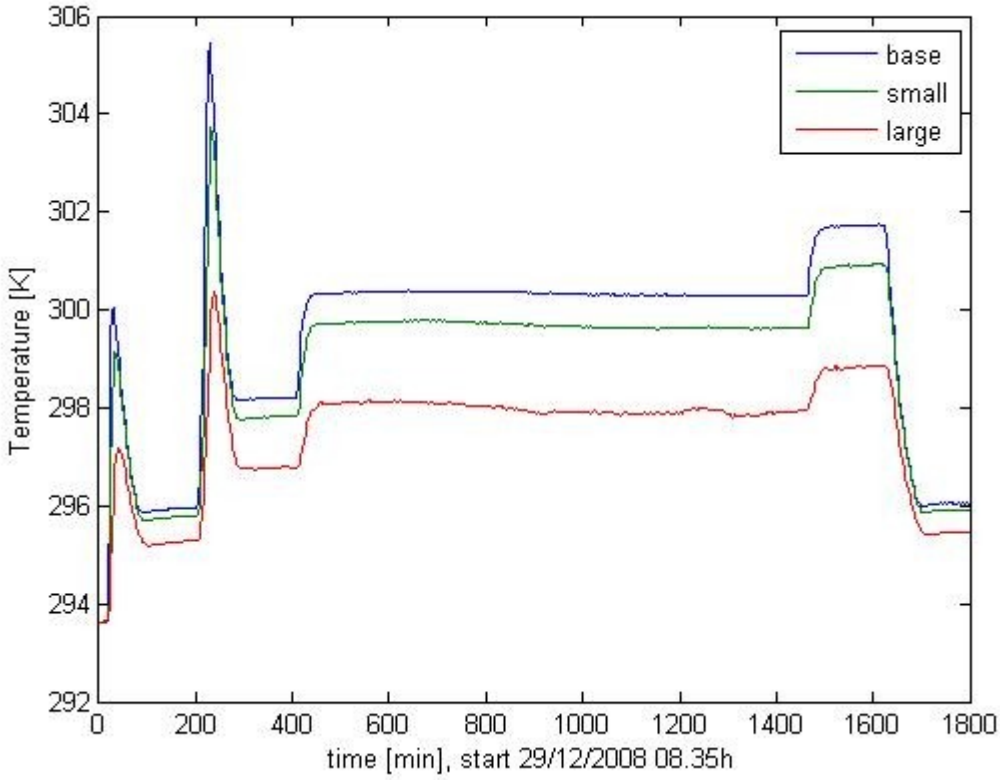

Figure 7.2 Temperatures at three points on the interferometer set-up

Temperatures were taken every three minutes. The heater control unit was set to multiple temperatures. See Table 7.2 for details. Temperature measurements were started on 29th December 2008 at 08.35h and ran until the following day 14.35h.

Table 7.2 Times and temperature settings during the test

Time	Temperature
08.35 29/12/2008 (0 min)	22°C (spiked first)
11.57 29/12/2008 (202 min)	25°C (spiked first)
15.24 29/12/2008 (411 min)	28°C
09.00 30/12/2008 (1405 min)	30°C
11.38 30/12/2008 (1623 min)	22°C

Several interesting things are seen here.
First of all, attention should be given to the offset seen between the temperature setting as given in Table 7.2 and the temperatures seen in Figure 7.2. At the first two sets of equilibrium data points the temperature as given in Figure 7.2 is higher than it should be according to the heater control, while at the last two it is lower. This must correspond to the way the set-up was heated. The first two times, due to an error, the heater first tried to heat up to over 40°C. At the times when this was corrected, the set-up overall temperature had reached a too high value.
Second, the temperature difference between the three measurement points draws our attention. This indicates a thermal gradient. The highest temperatures are seen at the mirror and the lowest at the highest sample. This difference can be up to almost 3K between the mirror and the largest sample.
Thirdly, the time it takes to stabilize to a temperature can be as high as 2 hours. The change in temperature is almost immediate for all sensor points, but the largest sample does take longer to stabilize. This is especially so when we let the system cool down to 22°C again.
This method of heating is not suitable for any further measurements we wish to take. For good measurements no thermal gradient should be allowed. Together with our already mentioned need for vacuum, this leads us to other forms of heating. This will be discussed in section 8.2.

Subsection 7.2.3 interferograms
A last concern we had to control was how to get our interferograms exported to MATLAB. The automated process with which the interferograms were made, were saved in an IntelliWave specific format. Luckily, afterwards it is possible to save the interferograms again in another, more standard, format (.jpg). This had unfortunately to be done by hand. By the time this report was written, a reader had just been developed to automate the exportation of the interferograms into a binary format [As09].
Figure 7.3 gives an example of the interferograms as recorded. The large circular area which is slightly truncated at the bottom is the image of our reference mirror. The five smaller circles are from the five BK7 samples we placed on the mirror. The red numbers indicate the sample number. There is no particular reason for this placing.

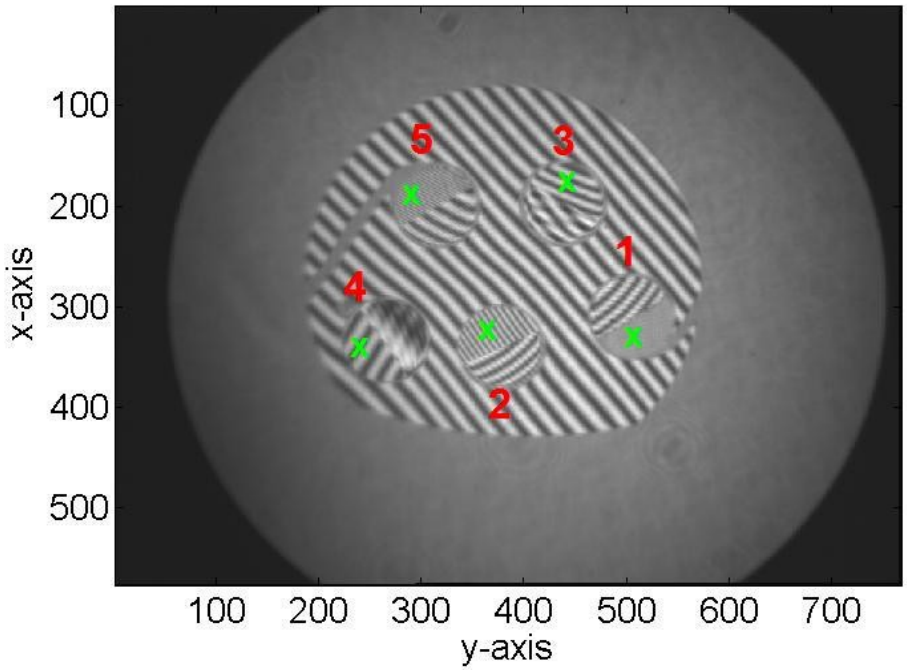

Figure 7.3 Example of the interferograms taken with the current set-up on 29th and 30th December 2008

A clear division in two parts is seen in each sample image. The 100% reflective coated sides have been marked with a green 'x'.
Without a wedge or anti-reflective coating on the uncoated parts of the samples, it is difficult to be certain whether the fringes we see there are from the front or the back plane or due to internal fringing. Careful alignment was necessary. Still, all samples show double fringe patterns. Sample #3 shows the clearest fringing from the backplane.
Sample #1 and sample #5 have very faint fringing on their reflective sides. The fringe spacing is too small for the pixel resolution.

Section 7.3 Analysis of the measurements
Figure 7.3 shows many fringes. These fringes were introduced because we wanted to investigate the systems response to heating. Any deviations or turbulence will be better visible when more fringes are present in the interferogram. For the 'real' measurements we will minimize the number of fringes, since fringing indicates an offset from a horizontal plane. Our reference mirror should be horizontal.

Given the known, some times crude, values of the CTE and IoR of BK7 and the CTE of Zerodur, we can make predictions about the phase shift we can expect and whether this phase shift should be visible in our interferograms. We will derive these predictions for sample #3, since we are most confident about the alignment there.

Table 7.3 Representative values of CTE and IoR of BK7 and CTE of Zerodur

	Value	Reference
CTE BK7	86e-7 K^{-1}	[SBK7]
CTE Zerodur	3e-6 K^{-1}	[SZer]
IoR BK7	1.51509	[Gh98]

Equations 5.4 and 5.8 give the change in phase deviation that we should observe. In the case of our ΔT=3K temperature shifts, we would expect a change in phase deviation $\Delta\phi$ of -1.70*10^{-3} [2π rad] for the coated half and $\Delta\phi$ = -6.82*10^{-3} [2π rad] for the transparent part.
The dynamic range of the interferometer intensity read-out is 8 bits. This corresponds to phase steps of approximately 5*10^{-3}. These phase steps are larger than the change in deviation we have just predicted. We will most likely not observe the change in phase deviation, but we can still investigate the systems response to heating.
The change in phase deviation will increase with larger temperature changes, thicker samples, or when investigating materials with higher CTE values. The best choice will be increasing the thickness. Increasing the temperature steps could invalidate our basic assumption from Chapter 5. Nor can we only investigate materials with high CTEs.

On the 29th we recorded 45 interferograms, each spaced 10 minutes apart, starting at 8.45h. During this time the temperature was stepwise increased as explained in Subsection 7.2.2. During the times that the temperature was being increased, the interferograms showed deformations in their fringe patterns, indicating non-uniform thermal distributions, and significant turbulence. When the temperatures had stabilized however, the interferograms no longer showed these deformations. The temperature stability was within the tolerance of our requirements, although their absolute value was of course not correct.
As a detailed indication of the stability of the interferograms, from 5 positions (same pixel) the phase was plotted as a function of the subsequent interferograms (Figure 7.4). These positions are two positions in the centre (mirror), on the reflective sides of samples #3 and #2, and on the uncoated side of sample #3. At thermal stability one expects the phase to remain constant. As is seen from the figure, this is certainly not the case. The two vertical bands (interferogram numbers 10 to 20 and 30 to 40) correspond to the first two thermally stable regions as depicted in Figure 7.2.

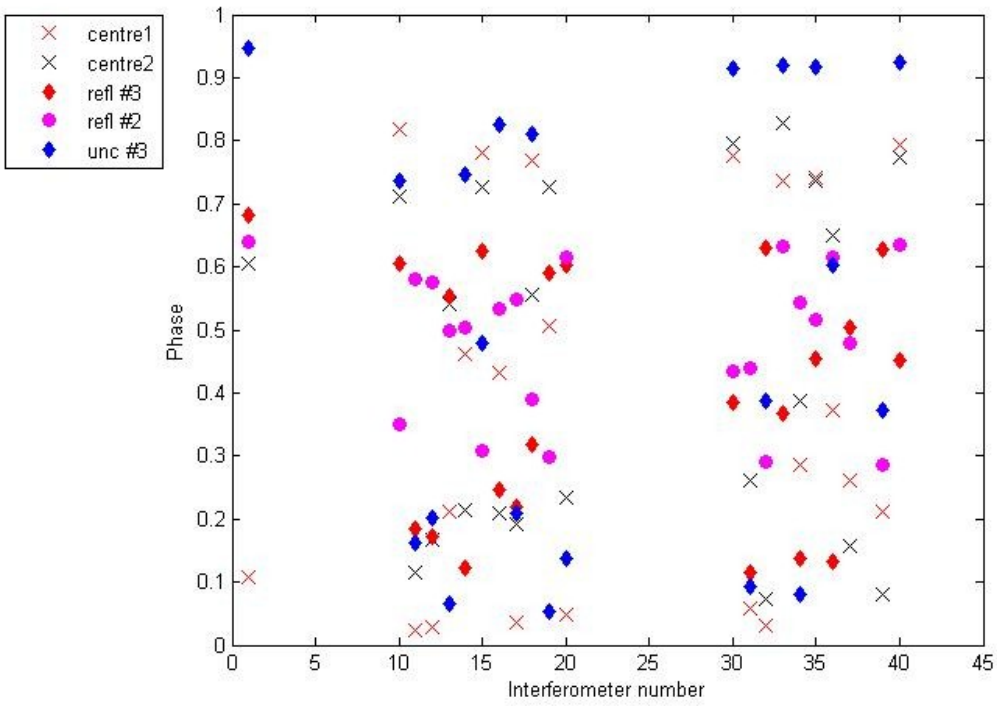

Figure 7.4 The phase at 5 positions in the interferograms with thermal stability

Gaussian noise might be present on these interferograms. So we have also fitted the areas around the five positions we chose with a two-dimensional waveform (Equation 7.1). An example of the fit is shown in Figure 7.5. The left panel shows the selected part of the interferogram, in this case the centre, and the right panel shows the resultant fit. Such a fit was made around all five positions of all interferograms that were recorded at thermal equilibria.

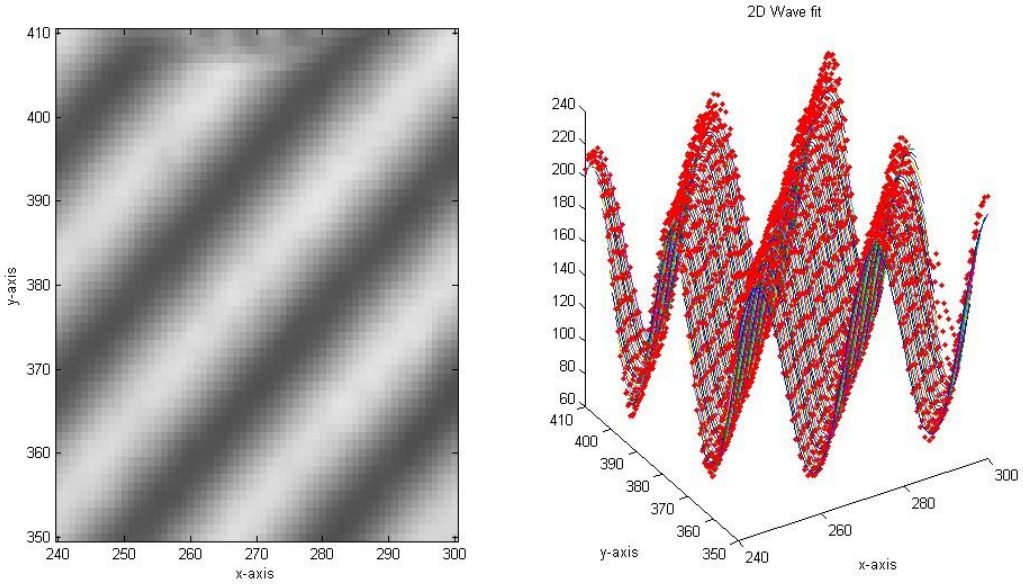

Figure 7.5 2D waveform fit to fringes on the interferogram

$$f(x,y) = c_1 + c_2 \sin(c_3 x + c_4 y + c_5)$$

Equation 7.1 2D waveform

This did not improve the stability at those points however as can be seen from Figure 7.6.

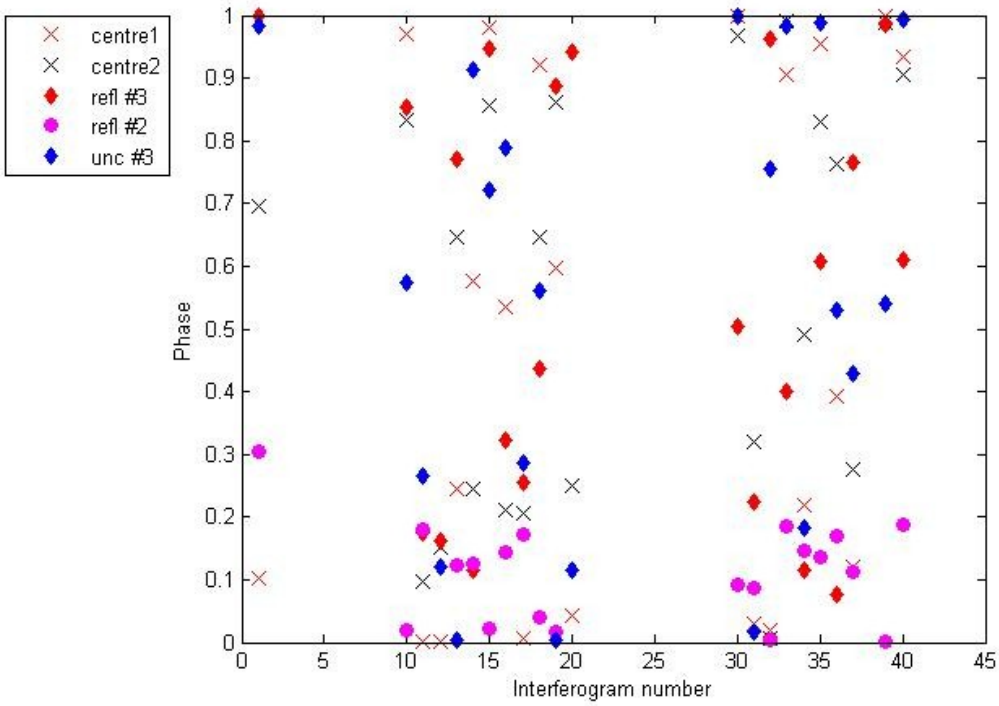

Figure 7.6 The phase at 5 positions in the interferograms with thermal stability after fitting

We believe that two causes might be responsible for our lack of stability; turbulence and a problem with the phase shifter.
Turbulence is of course still present, even though its effects are too small to see now with the naked eye. Measurements within a vacuum chamber will have to give the conclusive answer to this assumption.
However, another problem was found in the control of the interferometer. Namely, it was discovered that the phase shifter does not return to the same phase when taking several interferograms one after another.

Section 7.4 Discussion
Currently the interferometer doesn't seem capable of the stability we need for these measurements. Part of this problem is undoubtedly related to the effects of turbulence and the thermal gradient we have discussed. A large part of the problem may also have to do with the phase shifter.
The intensity resolution of the interferometer is approximately equal to the changes in the phase deviations our samples would induce. The choice of temperature steps, thickness or material may increase the changes in phase deviations to above the resolution threshold.
We remain hopeful that this method will generate results in the future, but realize that much work is yet to be done.

Chapter 8: Design

In this chapter we will look at the preferred designs for the two methods we have used in this research. The components must be chosen to meet the optical and mechanical requirements as set out in Chapters 4 and 5. The test measurements as described in chapters 6 and 7 have given us some strong indications for the do's and don'ts in the design selections.

The goal of the design is, as was stated in section 2.1, the measurement of the IoR at cryogenic temperatures with an accuracy of 10^{-5} and at wavelengths from 0.3 to 25 µm. To reach cryogenic temperatures the design will have to include a form of cooling. This gives further constraints on the design selections.

Section 8.1 Fabry-Pérot interferometry design

The spectrometer at ASTRON has the option to give an external beam. This in very fortunate, since it will allow us greater freedom in the design of the measurement set-up. Following [Be07] the design of Figure 8.1 is proposed. The light from the spectrometer is led through an external port, into a cryostat in which the sample is placed and onto the detector.

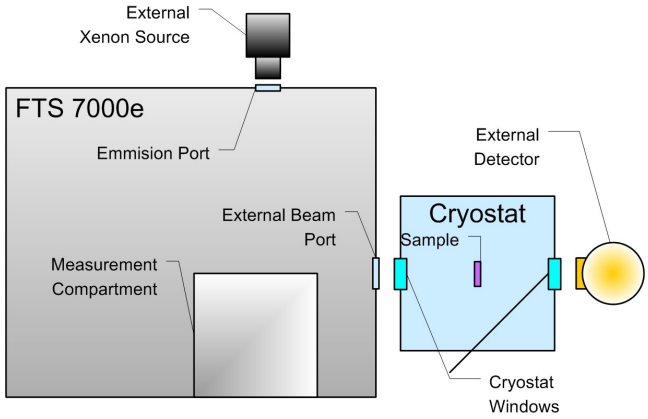

Figure 8.1 Proposal for the design of the spectrometer set-up to measure the IoR with etalon samples

This design has several advantages. First of all it frees us from the limitation of the small measurement compartment. The use of a cryostat, with a complete thermal cycle, is a costly and especially time consuming process. It is advantageous to measure multiple samples, either of different thicknesses or of different materials, during the same cycle. Any mechanism to hold these samples would never fit easily into the internal measurement compartment.

Secondly, this design also has room to include some form of beam adjustment. This will be necessary as the cryostat window together with aberrations in the light beam could result in angular deviations of the beam at the sample.

Thirdly, we will need multiple windows as we will discuss in Subsection 8.1.3. Again, an exchange mechanism would not fit into the internal measurement compartment.

Lastly, all components of the spectrometer can be used in this design. Both the internal and external light sources and the beam splitters can be used as they normally would be and the detectors are also operable outside the detector compartment.

The individual components of this design will now be discussed in further detail.

Subsection 8.1.1 Spectrometer

We have selected several hardware (Table 8.1) and software settings with which to span the whole spectral range wanted. Some overlap is seen in the wavelength range, this will ensure a smooth transition between the different settings.

Table 8.1 proposed spectrometer configurations (hardware)

	source	Beam splitter	Detector	Range [cm^{-1}]	Range [µm]
FIR	Standard ceramic	Mylar 6.25µm	DTGS	600 – 100	16.7 - 100
MIR1	Standard ceramic	KBr	DTGS	6000 – 400	1.67 – 25
NIR2	Tungsten halogen	NIR-Quartz	DTGS	10000 – 2800	1 – 3.57
NIR1	Tungsten halogen	NIR-Quartz	Silicon	20000 – 8600	0.5 – 1.16
Vis	Xenon (external)	UV-Quartz	Silicon	25000 - 10000	0.4 – 1
UV	Xenon (external)	UV-Quartz	PMT	54000 - 15500	0.19 – 0.65

Further settings on the spectrometer that need to be set in the software program are the aperture, resolution settings and apodization function. The aperture should be as small as possible to create a well defined beam while ensuring enough light for the spectrometer to stay away from the noise levels. The maximum acceptable aperture will probably be 1 cm^{-1}. The resolution should always be set to be 0.25 cm^{-1}. The apodization function should be set to 'NB medium' as was explained in chapter 6.

Subsection 8.1.2 Cryostat
At ASTRON no cryostat is available which is suitable for our design. A custom cryostat will have to be build.
The cryostats dimensions are defined by the dimensions of our sample holder. Further constrains on the design come from the placement of the windows and cooling mechanism.
Ideally the cryostat windows must be kept as small as possible to reduce pressure deformation. Preferably they are also circular in shape, again to reduce pressure related stresses. The diameter of the external port of the spectrometer is 63.5 mm and it is placed at 127mm height (bottom rim). The cryostat's window facing the spectrometer should be placed at the same height and be of the same size. The second window can be smaller. The entrance pupil of the detector has a diameter of only 30mm. It should be aligned in a direct line to the first window.
The cryostat must be able to reach and maintain a high vacuum. This is normal for most cryostats.

Subsection 8.1.3 Choice of cryostat window material
The cryostat needs multiple windows of different materials to cover the whole wavelength range. Otherwise the cryostat would need to be warmed up every time another window is needs to be installed. No material exists which is transparent over the entire wavelength range. The number of windows needed will depend on the transmission regions of the chosen window materials. To keep a simple optical alignment the walls holding the windows need to be able to rotate (within a limited angle).
The cryostat windows are further a prime example of optical elements in the light path which give undesired effects. The windows themselves will also exhibit etalon behaviour.
Each window will have a minimum thickness needed to sustain the pressure difference. The thickness of the window will lead to a secondary fringe pattern (Equation 4.10). If the window shows strong fringing, it can throw doubt on the source of the observed spectrum. This doubt can however be lifted if the reflection coefficient of the window is low. A low reflection coefficient results in a small height difference between a fringe top and bottom in the transmission spectrum. That way any fringing from the cryostat windows will be overpowered in the final spectrum by the fringing of the sample. A low reflectivity can be achieved by coating the windows with a broad spectrum anti-reflection coating.

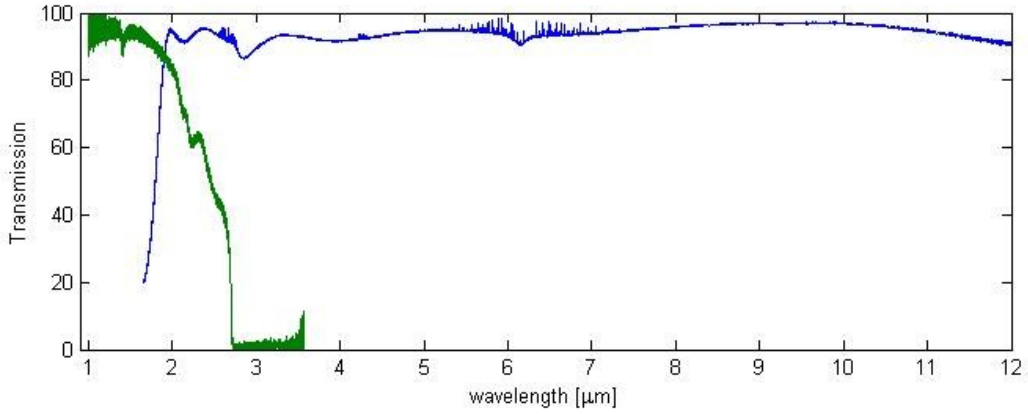

Figure 8.2 Transmission spectra of two cryostat window materials
Green: fused silica window, Blue: ZnSe window with AR coating

An example of the above argument is shown in Figure 8.2. The green spectrum belongs to a fused silica window which is often used as a cryostat window material. Besides the loss of transmission above 2.8 µm, the height difference, indicator of strong fringing, is much larger than the accompanying results from the ZnSe window. We were unable to obtain accurate results with the fused silica windows. The ZnSe window however was coated with an anti-reflective coating. The spectrum shown here was truncated for scaling purposes, but the window is usable from 2 to 22 µm.

As can be seen in Figure 8.3, the inclusion of the ZnSe cryostat windows has deformed the deviation a little. This is clear from comparison between Figure 6.4 and 8.3. Both are results are derived from the 1.5mm sample at the MIR1 setting. This deformation primarily occurs at wavelengths below 5µm.
Comparative analysis between the two spectra has found that the locations of the fringe maxima slowly drift apart, most notably at the lower wavelengths. This effect is due to the different angle under which the etalon sample is illuminated when the ZnSe window is included. In Equation 4.11 we saw that the locations of the fringe maxima is inversely related to cos(θ). The light inside the measurement chamber is inherently convergent. When it hits the window, it will get refracted and light will hit our sample under another angle. This effect is most notable at the lower wavelengths, because the drift propagates away from the location where we restrained the IoR (around 7µm), and because the fringe locations are closer together at the lower wavelengths.
This proves again our need to include some form of beam adjustment in the design.

Another window material will have to be found for the lower wavelength measurements.

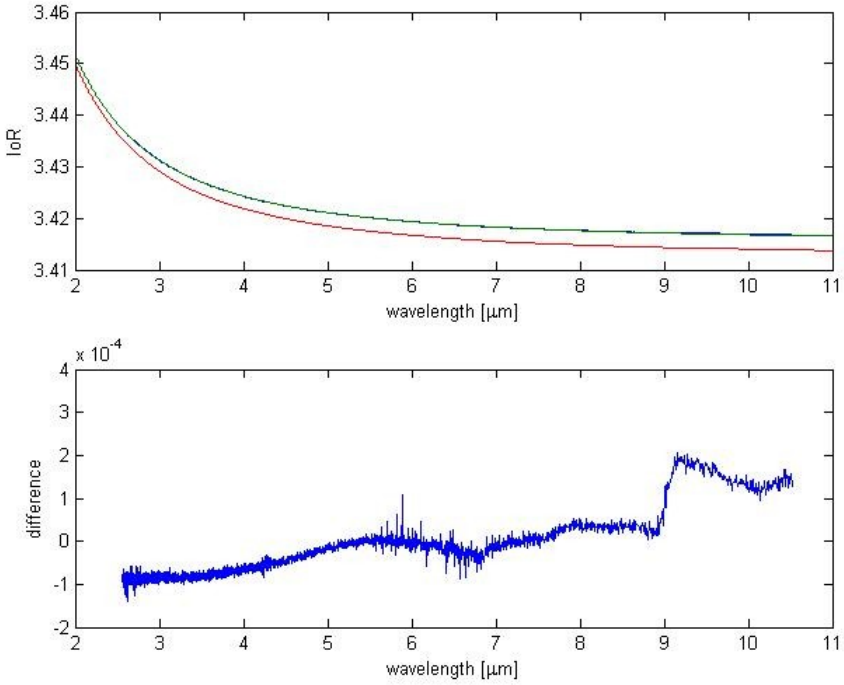

Figure 8.3 Theoretical vs. calculated IoR with their difference.
Results for 1.5mm sample (with ZnSe window) and MIR1 settings

Subsection 8.1.4 Detector casing and connections
A special compartment will have to be built for the detectors. They cannot be placed inside the cryostat, since they are designed to operate at room temperature. The dimensions of the compartment are not critical. The only critical issue is the possibility to flush the compartment with dry air and a good alignment with the spectrometer.
To reduce the risk and disadvantages of atmospheric influences (i.e. water vapour and carbon dioxide), the spaces between the cryostat and spectrometer and detector must be continuously flushed with dry air. A simple, air tight cylinder connecting the different components will suffice. The cylinder between spectrometer and cryostat can be flushed with the dry air environment of the spectrometer. The cylinder between cryostat and detector and the detector compartment would need an inlet for the dry air flow.

Subsection 8.1.5 Sample holder
The most practical design of the sample holder would be circular, with some electron-magnetic way of changing the position. We will follow the design of the sample exchange mechanism idea for the MIDI instrument[4]. The change mechanism must be accurate enough to position the samples directly in the

[4] More information on MIDI: http://www.eso.org/projects/vlti/instru/midi/index.html

light path and maintain a zero-offset in angle from perpendicular alignment. The MIDI design will ensure these requirements.
The holder must be placed in the cryostat such that a single sample is in the light path of the spectrometer to detector.

Subsection 8.1.6 Thermal control
To bring the temperature down to 15K, cooling with liquid nitrogen is not sufficient. This will bring the temperature down to 77K. To bring the temperature down even further other techniques will have to be employed. Liquid helium would bring the temperature down to 4K, but it is not readily available at ASTRON. Otherwise a close-cycle cooler or pulsed-tube cooler could be used.
The centre of the sample holder can serve as the main thermal contact for the cooling mechanism. This will ensure uniform cooling of all samples.
For the temperature control we can use 4 wire high resistance RTDs and an HPVee program written in-house. The temperature sensors themselves also need to be within their operating range. A wide selection of RTD sensors is available which operate specifically at cryogenic temperatures and with the accuracy needed for our measurements. Installing several different types will ensure the entire temperature range will be measured correctly.
It is not possible to measure the temperature at the sample which is in the light path, since that would block the light. To have a good constraint on the temperature, a dummy sample could be placed in the sample holder to which sensors could be attached. This dummy variable should be some bad thermal conductor; then it will always be the last position to reach thermal equilibrium.

Table 8.2 summarizes the proposed dimensions of the individual components in de Fabry-Pérot interferometry design.

Table 8.2 Dimensions of the Fabry-Pérot interferometry design

component	Size / diameter	Remarks
External beam port	63.5mm	
Cylinder spec-cryo	63.5mm	
Cryostat windows 1	>63.5mm	Plane parallel, AR coated
Cryostat		Depends on size sample holder
Sample holder aperture	1 inch	
Cryostat window 2	30mm	Plane parallel, AR coated
Cylinder cryo-det	30mm	Dry air inlet
Detector casing	20cmx20cmx20cm	

Section 8.2 Imaging interferometer design
The Wyko interferometer will form the heart of the Imaging interferometer design. Our initial measurements suffered from flaws in the interferometer which prevented us from obtaining accurate results. Still, the basic design can be maintained.
The basic set-up of the samples will remain as first described in Chapter 7 and depicted in Figure 8.4. The light from the interferometer is first deflected by a movable mirror angled to the set-up on the cryostat floor. This set-up consists of a reference mirror on which the samples are placed. The tip-tilt mechanism on which the reference mirror rests will need to be bolted down to minimize thermal deformation.
This design has several key advantages. Keeping the samples horizontal makes it easy to change or reposition samples. The number of samples is only limited by their sizes relative to the beam surface (~(6 inch)^2), and not to the number of positions in any vertical construction. By placing the samples horizontally, gravity will keep the samples in place without an elaborate mechanical construction, introducing no stresses on the samples and cutting costs. We have shown in Subsection 7.2.2 that gravity is enough to ensure thermal contact.

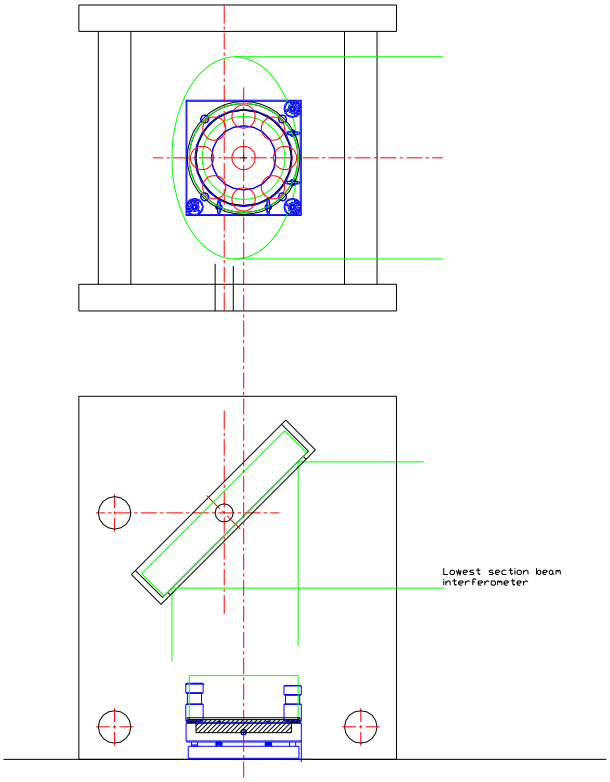

Figure 8.4 Schematic proposal for the design of the interferometer set-up to measure the IoR with samples of different height

Subsection 8.2.1 Interferometer
The interferometer can be operated in its general mode. The interferometer must be set to a light intensity which is as high as possible while avoiding overexposure. The zoom and focus should be set as to optimize the image. After the settings have been set, they should not be changed again. This would only increase the difficulty of the comparative analysis later.

Subsection 8.2.2 Cryostat
The samples, mirrors and tip-tilt mechanism will need to be incorporated into a cryostat. This is needed to reach the cryogenic temperatures, but also has the secondary advantage of eliminating the turbulence resulting from the heating and cooling process. This cryostat must be placed as closely as possible to the interferometer to minimize any secondary turbulence effects.
A cryostat exists at ASTRON which was in part designed specially for cryogenic interferometer measurements. Its window has a diameter of 150mm (~6 inch). The cooling mechanism is located on the far wall. Our samples should be placed there.

Subsection 8.2.3 Mirrors
The reference mirror must be kept as flat as possible. Otherwise it becomes impossible to accurate determine any changes in fringe deviations. When flatness is ensured, the reference mirror material should be selected to heat or cool uniformly. The angled mirror should be kept thin and with a low CTE, so any thermal expansion or contraction will be minimal. Otherwise the positions on the interferometer will shift.
The diameter of the two mirrors is linked; the angled mirror must always be larger than the reference mirror. The largest meaningful diameter of the reference mirror is 6 inch, the interferometer beam diameter. The diameters of the current mirrors are 150mm for the angled mirror and 83.5mm for the reference mirror.
The mirrors must be flat, minimally $\lambda/10$.

Subsection 8.2.4 Tip-tilt mechanism
The tip-tilt mechanism currently used in the set-up has a usable diameter of 83.5mm. It was purchased at ThorLabs. It was not produced for use at cryogenic temperatures and its applicability will have to be investigated. If a larger reference mirror is wanted, this mechanism will be useless in any case.

Subsection 8.2.5 Thermal control
When changing the temperature, care must be taken to get uniformly heated/cooled samples. Zerodur, the mirror material, has a low thermal conductivity. This means that heating is a slow process and that thermal losses really have to be minimized. In vacuum thermal losses can only occur through radiation. The temperature stability and uniformity have to be assured. A 'heat pocket' can be maintained by including heat shields in the cryostat.
For the temperature control we can again use 4 wire high resistance RTDs and an HPVee program written in-house.

Table 8.3 shows the proposed dimensions of the individual components in de imaging interferometer design.

Table 8.3 Dimensions of the imaging interferometer design

component	Size / diameter	Remarks
Cryostat window	150mm	available
Cryostat		ASTRON's 'cryobox'
samples	18.4mm	Coated 100% Refl / AR
Angled mirror	>150mm	Flatness λ/10 or better
Reference mirror	150mm (current 83.5mm)	Flatness λ/10 or better

Section 8.3 Measurement Procedure and Software
Our measurements consist of two parts; the measurements with the interferometer and the measurements with the spectrometer. Ultimately the goal is to fill the IoR parameters space of wavelength and temperature.
In principle measurements can be done in parallel for the interferometer and spectrometer, but the final results of the spectrometer measurements are dependent upon the results of the interferometer. For the interferometer and spectrometer measurements, the control software in both cases has the possibility to automate the measurements.

A software package written in MATLAB has been developed to analyze the measurements. Together with documentation is this package available at ASTRON. The final programs to analyze the imaging interferometer measurements are still missing. The (completed) basic components of the package are the following.
Once the Fabry-Pérot spectra have been collected with the control software, the spectra can be exported in a .csv format. Code has been written to import the spectrum, determine the fringe maxima and calculate the IoR vector.
Similarly has some code been written for the interferograms. These can be exported as .jpg files. Code has been written to fit the fringes, however this will most likely need further work once our measurements get better.
Finally, some code exists which can give an estimate of the uncertainty. This is based on the input values and the theorized error analysis as derived in Chapter 4 and 5.

Conclusions and Outlook

Given the current projects and ambitions expressed by the astronomical community, swift and accurate determination of the IoR at cryogenic temperatures is a must.

Our goal in this study was to develop a refraction measuring device able to measure the IoR of solids within the following framework:

- wavelength range 300nm - 25µm
- temperature range 20K – 300K
- accuracy to at least the 5^{th} decimal place

We have presented two methods capable of measuring the IoR at cryogenic temperatures; minimum deviation refractometry and the Fabry-Pérot interferometry method. We have further investigated the development of a refraction measuring device based on this second method. Our main arguments were the ability to cover a wide wavelength range in a single measurement and the availability of the equipment. However, one alternative single wavelength measurement of the IoR is needed to constrain the fringe order.

A new interferometer set-up has been proposed which could give this single wavelength measurement and the coefficient of thermal expansion of the material as well. The method is based on the optical path lengths dependence on IoR between light travelling through a medium and light travelling through vacuum.

We have presented initial measurements at 27°C made using the Fabry-Pérot method. These methods showed a deviation of order 10^{-4} when compared with literature values and also a reproducibility of order 10^{-4}. We discussed that a better constraint on the angle under which light hits the samples will increase the accuracy. The reproducibility will most likely increase by adding more scans together into a single spectrum.

Initial measurements were also done with the interferometer set-up between 22°C and 30°C. The intensity resolution of the interferometer is approximately equal to the change in the phase deviations our samples would induce. Choosing larger temperature steps, thicker samples or materials with larger CTE will bring the changes above our resolution threshold. Of these choices manufacturing thicker samples holds our preference.

Hardware designs were discussed for both methods. These designs incorporated the lessons we has learned from the initial measurements. They also included the thermal control needed to span the entire temperature range as set down in our goals.

We conclude that the Fabry-Pérot method is a viable method with which to measure the IoR, also at cryogenic temperatures. Its downside is the need to constrain the fringe order.

Further research on the interferometer set-up will have show whether this method is capable of delivering this constraint.

Further work will have to be done before this refraction measuring device is operational. Our outlook on future work can be divided into the following tasks.

- Building the designed set-up of the Fabry-Pérot interferometry method
- Testing the Fabry-Pérot design over the complete wavelength and temperature ranges
- Detailed investigation into the Steepest Descent Method as a means of constraining the fringe order
- Further investigation into the interferometer set-up and especially the workings of the interferometer itself

The first three tasks of the future work could be assigned to personnel already working at ASTRON. For the final design of the Fabry-Pérot set-up a mechanical designer is needed to draw up detailed designs. The assembly and testing of the set-up can be done by an engineer. Further investigation into the interferometer is currently already under way by a system engineer.

For the investigation into the Steepest Descent Method someone will have to be found with extensive knowledge of mathematics and programming experience.

References

[As09] Astron in-house developed code to extract interferogram from IntelliWave files into binary files. Not named yet, 2009

[Be07] Beecken, J., *Conception of the Index of Refraction Measurement Instrument (IRMI)*, ASTRON 2007

[Br04] Brown, W.R., Epps, H.W. and Fabricant, D.G., *The cryogenic refractive indices of S-FTM16, a unique optical glass for near-infrared instruments*, arXiv:astro-ph/0404414v1, 2004

[Bu05] Burden, R.L., Faires, J.D., *Numerical Analysis*, Thompson Brooks/Cole, 8th edition 2005

[Gh98] Ghosh, G., *Handbook of Thermo-Optic Coefficients of Optical Materials with Applications*, Academic Press, 1998

[Gu03] Gupta, R. and Kaplan, S.G., *High accuracy ultraviolet index of Refraction measurements using a Fourier Transform Spectrometer*, J.Res.Natl.Inst.Stand.Technol., 108, 429-437, 2003

[He02] Hecht, *Optics*, Addison Wesley 4th international edition, 2002

[Ka98] Kaplan, S.G. et al., *Fourier transform refactometry*, SPIE Vol. 3425, July 1998

[Kapc] Kaplan, S.G., *private communication*

Le03] Leviton, D.B. and Frey, B.J., *Design of a cryogenic, high accuracy, absolute prism refractometer for infrared through far ultraviolet optical materials*, 2003

[Le05] Leviton, D.B., Frey, B.J. & Kvamme, T., *High accuracy, absolute, cryogenic refractive index measurements of infrared lens materials for JWST NIRCam using CHARMS*, 2005

[Pl75] Platt, B.C., Icelogle, H.W., Harvey, J.E., Korniski, R. and Wolfe, W.L., *Technique for measuring the refractive index and its change with temperature in the infrared*, J.Opt.Soc.Am., 65 1264-1266, 1975

[SBK7] http://www.glassdynamicsllc.com/BK7%20Material%20Data%20Sheet.htm

[SZer] http://www.schott.com/optics_devices/german/download/tie37_thermal_expansion_of_zerodur.pdf

[Sp08] Spano, P. et al., *Design and development of a cryogenic high-accuracy refractometer*, 2008

[Te90] Tentori, D. and Lerma, J.R., *Refractometry by minimum deviation: accuracy analysis*, Optical Engineering 29(2), 160-168, 1990

[Va08] Vannoni, M. et al., *Measuring the refractive index of vitreous materials at cryogenic temperature with a spectrometer*, Meas.Sci.Technol., 19, 085304, 2008

[Wo80] Wolfe, W.L., Debell, A.G. and Palmer, J.M., *Cryogenically cooled sensor technology*, Proc. SPIE, vol. 245 164-172, 1980

[Wiki] Wikipedia contributors, *Fabry-Pérot interferometer*, Wikipedia, The Free Encyclopedia, http://en.wikipedia.org/w/index.php?title=Fabry-P%C3%A9rot_interferometer&oldid=236343277 (accessed July 17, 2008)

[Ya06] Yamamuro, T. et al., *Measurement of refractive indices of 20 optical materials at low temperatures*, Opt.Eng. 45(8), 083401, 2006